TOPICAL REVIEW

Theory of nonlinear charge transport, wave propagation, and self-oscillations in semiconductor superlattices

L L Bonilla

Departamento de Matemáticas, Escuela Politécnica Superior, Universidad Carlos III de Madrid,
Avenida de la Universidad 30, 28911 Leganés, Spain
and
Unidad Asociada al Instituto de Ciencia de Materiales (CSIC), Spain

Abstract
Nonlinear charge transport in semiconductor superlattices under strong electric
fields parallel to the growth direction results in rich dynamical behaviour
including the formation of electric field domains, pinning or propagation of
domain walls, self-sustained oscillations of the current and chaos. Theories
of these effects use reduced descriptions of transport in terms of average
charge densities, electric fields, etc. This is simpler when the main transport
mechanism is resonant tunnelling of electrons between adjacent wells followed
by fast scattering between subbands. In this case, we will derive microscopically
appropriate discrete models and boundary conditions. Their analyses reveal
differences between low-field behaviour where domain walls may move
oppositely or parallel to electrons, and high-field behaviour where they can only
follow the electron flow. The dynamics is controlled by the amount of charge
available in the superlattice and doping at the injecting contact. When the charge
inside the wells becomes large, boundaries between electric field domains are
pinned resulting in multistable stationary solutions. Lower charge inside the
wells results in self-sustained oscillations of the current due to recycling and
motion of domain walls, which are formed by charge monopoles (high contact
doping) or dipoles (low contact doping). Besides explaining wave motion and
subsequent current oscillations, we will show how the latter depend on such
controlling parameters as voltage, doping, temperature, and photoexcitation.

1. Introduction

Semiconductor superlattices (SL) are unique nonlinear systems as regards electric charge-
transport properties. To form a SL, several identical periods formed by two layers of compatible
semiconductor materials (e.g., GaAs and AlAs, with similar lattice constants) are grown in
the vertical direction, say [2, 5, 33]. The conduction band of an infinitely long SL looks like

a one-dimensional crystal formed by a succession of quantum barriers and wells (AlAs and GaAs in our previous example) [5]. In typical experiments on vertical transport, a finitely long, doped or undoped SL is placed in the central part of a diode (forming an n$^+$–n–n$^+$ or a n–i–p structure) and contacts are attached at the two ends thereof. Depending on bias conditions, SL configuration, doping, temperature, and other control parameters, the current across the SL and the electric potential inside display a great wealth of patterns and dynamical behaviour, some of which we shall review in this article. What makes the SLs unique nonlinear systems is that, in certain regimes, they present features of spatially discrete systems, whereas their behaviour is more typical of continuous systems in other regimes. These different properties may be described by discrete or continuous balance equation models. Their derivation from first principles is not yet fully accomplished [83], and it is rather challenging from the point of view of statistical mechanics. Studies of fluctuation and noise phenomena in SL under strong electric fields may be starting only now [13]. These different facets of nonlinear charge transport in SL will we hope emerge in this review. In it, we will describe the more salient features of nonlinear dynamics in SL, emphasizing particularly wavefronts and wave propagation, which constitute the keystone of our present understanding. We will consider here weakly coupled SL only, in which the barrier width is much larger than the reciprocal of the typical electron wavenumber inside the barrier. In the opposite limit, nonlinear transport in strongly coupled SL can be often described by continuum balance equations or semiclassical Boltzmann equations inside minibands [73, 74]. Mathematically, this is similar to well-known theories for bulk semiconductors [18]. Of course, miniband approximations should break down at sufficiently high fields, and a better theoretical understanding is needed there.

As pointed out above, the scope of this review is limited, for we aim at understanding the basics of those nonlinear phenomena in charge transport in weakly coupled SL that are due to the formation of electric field domains in the SL. We will approach this by studying a class of spatially discrete models of vertical charge transport. Our discussion will be focused on wavefronts and wave propagation in discrete systems. Unlike in continuum models, wavefronts in discrete systems may fail to propagate when a control parameter takes values in certain finite intervals [24–27, 42]. This pinning of wavefronts is crucial to understanding their motion and stationary states in infinite or finite SL. Other aspects of wavefront motion crucial to understanding self-sustained oscillations of the current in a voltage-biased SL can be understood by using continuum limits of discrete models as approximations. Their accuracy should be contrasted with numerical solution of the discrete models and validated by experiments.

We believe that it is important to attain an understanding of nonlinear dynamics in SL charge transport that runs deeper than merely simulating model equations and checking whether theoretical predictions and experimental data agree. This is interesting not only for the field that we are reviewing, but also for other fields where spatially discrete models play a role. Among them, let us cite models of dislocations [14, 57], models of crack propagation [75] and friction in solids [30], sliding of charge-density waves [35], arrays of superconductor Josephson junctions [86], and propagation of nerve impulses along myelinated fibres [42]. To our knowledge, this review is the only existing one that tries to explain, in a mathematically consistent way, the nonlinear charge-transport phenomena observed experimentally and numerically in weakly coupled SL. Important aspects of superlattice physics not covered by our review can be found in the following books and review papers: growth processes and transport measurements in [33], electronic structure in [2, 5, 37, 76], different theories of charge transport in [72, 83]. The current status of the quantum kinetics of SL (under homogeneous electric fields and quasistationary conditions) can be found in the review by Wacker [83], that also contains a section on formation of electric field domains and a wealth of references.

The rest of this article is organized as follows. First of all, we will describe in section 2 a few key experimental results illustrating the interplay between discrete and continuous aspects of nonlinear vertical transport in SL. Then we will present widely used models thereof and comment on derivations from first principles in section 3. An understanding of aspects of nonlinear dynamics will be obtained by solving these models in different parameter regimes. Our discussion will be focused on wavefronts and wave propagation in discrete systems, which is the key to understanding the observed nonlinear dynamical phenomena. Unlike in continuum models, wavefronts in discrete systems may fail to propagate when a control parameter takes values in certain finite intervals [24–27, 42]. This pinning of wavefronts is crucial to understanding their motion and stationary states in infinite or finite SL, as we will explain in section 4. In sections 5 and 6, we will show how waves can be used to explain different phenomena observed in dc voltage-biased SL. In section 5, we explain the relocation of domain walls after a sudden voltage change. In section 6, we study self-sustained oscillations of the current through a voltage-biased SL and the roles of doping, temperature, photoexcitation, etc. In the final section, we will comment on several interesting open problems. Appendix A is devoted to deriving analytical expressions for the transport coefficients and contact currents (not found elsewhere at the time of writing), and appendix B contains considerations on the continuum limit of a discrete model with a more general constitutive relation for the tunnelling current density than the discrete drift-diffusion (DDD) model studied in this review.

2. Key experimental results

The current–voltage (I–V) characteristic curve of a weakly coupled SL presents the distinctive multibranch aspect shown in figure 1(a) when there is enough electric charge inside the SL. This charge may be produced by doping or irradiating the SL with appropriate laser intensity (thereby generating electron–hole pairs). The multiplicity of branches in the I–V curve is due to the formation of electric field domains, as explained below. When the electron density inside the SL is sufficiently low, the electric field is almost spatially uniform. The I–V curve is smooth and it has a number of peaks as depicted in the dotted photocurrent curve of figure 1(b) corresponding to an undoped reference sample with the same configuration as the doped sample. (The photocurrent is proportional to the number of electrons that arrive at the collector per unit time after a pulse excitation and can be measured by varying the current through a resistor in series with the SL [70].) These peaks of the current occur at field values at which the subbands of two adjacent wells are aligned. Take for instance the second peak in figure 1(b). If the applied field is $(\mathcal{E}_{C2} - \mathcal{E}_{C1})/(el)$ (e is minus the electron charge and l is the SL period), electrons in the lowest subband of a given well, $C1$, with energy $\mathcal{E}_{C1}$ in the absence of bias, tunnel resonantly across the barrier to the $C2$ subband of the adjacent well (with energy $\mathcal{E}_{C1}$ in the absence of bias). They then undergo scattering processes (with LO phonons, interface roughness, . . .) and fall to the $C1$ subband of that well. This process is called sequential tunnelling; see figure 2(a). Outside resonances, charge transport is less efficient, resulting in lower values of the current. Whatever the value of the charge in the SL, the bias regions between peaks of the current are called plateaus. The first peak is approximately located at a field equal to the scattering energy divided by el, while the second peak is approximately given by $(\mathcal{E}_{C2} - \mathcal{E}_{C1})/(el)$, and so on.

Provided that the charge inside the SL is large enough, a spatially uniform field configuration is unstable and a stationary field configuration having two electric field domains appears. A rough description of these domains is as follows. Assume that the bias is on the first plateau of the I–V curve and that both current and voltage are independent of time. The electron drift velocity is proportional to the photocurrent of the undoped reference sample
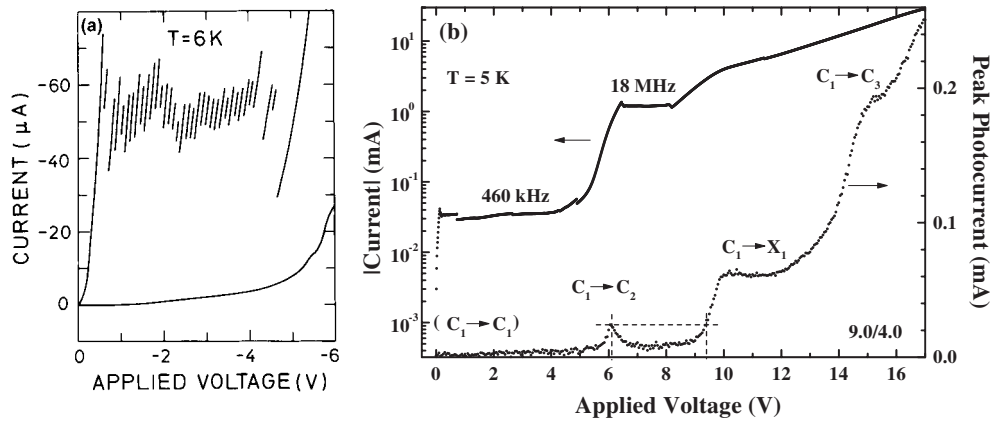
Figure 1. Current–voltage characteristic curves of GaAs/AlAs SL. (*a*) The multibranched characteristic for the first plateau of a negatively biased sample with $w = 9$ nm, $d = 4$ nm, doping $N_D^w = 1.5 \times 10^{11}$ cm^{-2}. The smooth curve for lower current corresponds to an undoped SL with the same configuration (reference sample) (reprinted from [32]). (*b*) The characteristic with flat plateaus for the same sample, positively biased over a larger voltage range. The dotted characteristic curve underneath is the peak photocurrent versus applied voltage obtained by time-of-flight experiments on the undoped reference sample (reprinted from [40]).
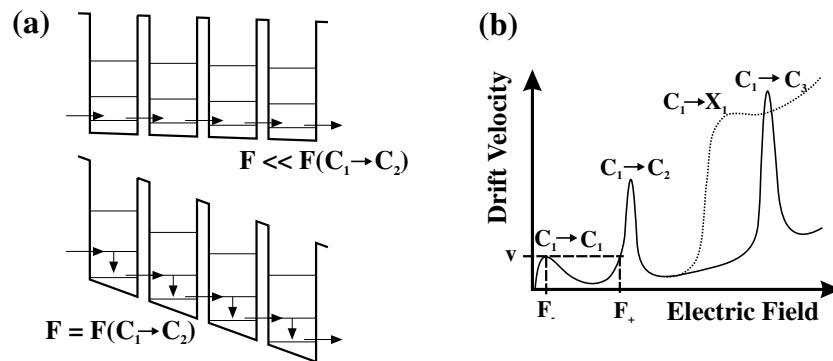

Figure 2. (*a*) The conduction band profile of a superlattice with three subbands in an applied electric field. (*b*) Drift velocity versus field characteristics of this superlattice consisting of the nonresonant background, the low-field maximum ($C_1 \rightarrow C_1$), and the first two resonant tunnelling maxima. The dotted curve indicates a possible shape of the $v(F)$ curve in the case of a $\Gamma \rightarrow X$ resonance located between the $C_1 \rightarrow C_2$ and $C_1 \rightarrow C_3$ resonances. The dashed line is explained in the text (reprinted from [40]).

in figure 1(*b*), which is schematically indicated in figure 2(*b*). Part of the SL (the first m SL periods) is at an almost zero field F_- and resonant tunnelling between $C1$ subbands of adjacent wells dominates. The rest of the SL ($N - m$ SL periods, where N is the total number of periods) is at the field F_+ having the same velocity (proportional to the photocurrent) as the $C1$–$C1$ resonant field F_-; see figure 2(*b*). F_+ is slightly smaller than that corresponding to the $C1$–$C2$ resonant tunnelling process described above; $F = (\mathcal{E}_{C2} - \mathcal{E}_{C1})/(el)$. The extent of the lower-field domain is given by the condition that $m F_- + (N - m) F_+ \approx (N - m)(\mathcal{E}_{C2} - \mathcal{E}_{C1})/(el)$, equal to the voltage across the SL. As shown in figure 3, we may have coexistence of different domain branches for a given value of the voltage. The field configuration at each branch differs
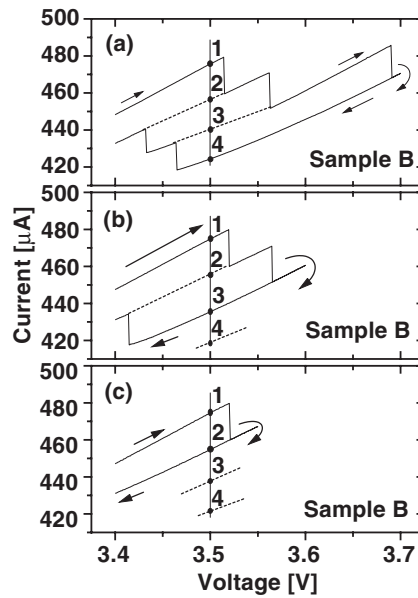
Figure 3. Details of the multistability of the stationary field configurations in figure 1(*a*) obtained by successive adiabatic up-sweeping and down-sweeping of the *I*–*V* characteristic curve. (*a*)–(*c*) correspond to different up-sweeping and down-sweeping processes designed to reveal different stable branches (reprinted from [39]).

in the extent of low- and high-field domains. The domain wall separating low- and high-field domains is at the last SL period for the first branch after the $C1$–$C1$ resonance in figure 1(*a*). Then $m = N - 1$. For the following branch, $m = N - 2$, and so on. The extent of the high-field domain is smaller for a branch having higher current value than for another one at the same voltage. Adiabatic up-sweeping and down-sweeping of the *I*–*V* curve shows hysteresis cycles and experimentally demonstrates multistability of different branches as shown in figure 3. The coexistence of two electric field domains inside the SL is confirmed by photoluminescence measurements [31].

At intermediate values of the charge inside the SL, the *I*–*V* curve is flat between peaks as depicted by the curve at larger current of figure 1(*b*). When time-resolved measurements of the current are carried out in these flat regions, self-sustained oscillations are observed, as in figure 4. In certain cases, experimental evidence shows that self-oscillations appear as recycling and motion of domain walls separating two electric field domains. This can be verified experimentally by indirect means because the current–time trace is directly measurable but the electric potential or field inside the SL is not. Typical indirect measurements are the time-resolved photoluminescence spectra. The photoluminescence intensity (shown as a greyscale in figure 4(*c*) such that darker regions correspond to larger intensity) is recorded for each time as a function of the wavelength or energy of light emitted due to electron–hole recombination. Let us assume that there are two electric field domains in the SL, one at zero field, so that electrons tunnel from the $C1$ subband of one well to the $C1$ subband of the next well, and the other at a field corresponding to $C1$–$C2$ resonant tunnelling. Recombination light emitted by wells in the high-field domain has less energy than light emitted at zero field due to the quantum confined Stark effect [53]. If most of the SL is at zero field, the photoluminescence spectrum will present a peak at higher energy than that corresponding to a SL most of which is at the $C1$–
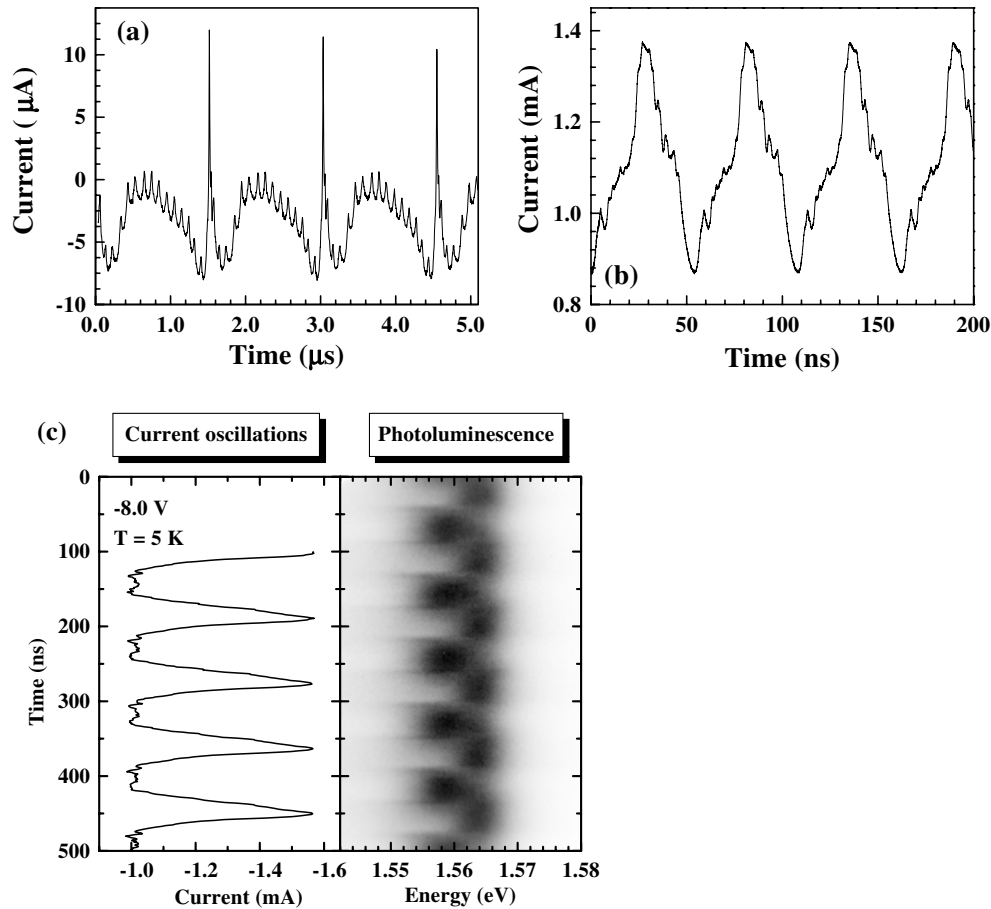
Figure 4. Time-resolved current oscillations for a GaAs/AlAs SL with $w = 9$ nm, $d = 4$ nm, $N_D^w = 10^{11}$ cm^{-2}. (*a*) The time-resolved signal showing current self-oscillations for a bias on the first plateau (2.77 V) at 6 K. Notice the high-frequency spikes superimposed on the self-oscillations. (*b*) The same, but for a voltage on the second plateau (7.3 V at 5 K): current spikes are much harder to observe (reprinted from [38]). (*c*) Comparison of time-resolved current oscillations and the photoluminescence spectrum for a bias on the second plateau (reprinted from [34]).

$C2$ resonant field. Thus the strength of the photoluminescence peaks gives an idea of the spatial extent of the corresponding electric field domains. Figure 4(*c*) shows that photoluminescence peaks corresponding to two domains (the values of the field at these two domains correspond to the $C1$–$C2$ and the $C1$–$C3$ resonant fields) alternate in strength, in phase with current self-oscillations. This suggests that the extent of these domains is periodically changing with time, as indicated by numerical simulations of the models presented later. An interesting feature of the self-oscillations in figure 4(*a*) is the presence of current spikes superimposed on the signal. Experimental and numerical evidence shows that each spike occurs as the domain wall moves from one SL well to the next. Then the number of spikes during each self-oscillation period indicates the number of wells traversed by the domain wall during its motion. In figure 4(*a*), the number of spikes in one period of the current–time trace is significantly lower (17) than the number of SL periods (40). This suggests that recycling and motion of domain walls is confined to part of the SL [40]. Theory and numerical simulations of discrete models [67, 83] (see below) show that current self-oscillations may be due to recycling and motion of two

different type of wave: accumulation wavefronts (which are moving charge monopoles) and pulses of the electric field (which are moving charge dipoles). The current–time traces and the corresponding electric field profiles of these two oscillatory states are different, and the main difference is as follows. Dipoles recycle in the injecting region and move until they arrive at the receiving region therefore, whereas monopoles first become appreciable well inside the SL and then move until they arrive at the receiving contact. Correspondingly, the current–time trace of dipole-type self-oscillations should exhibit a number of spikes close to the number of SL periods (40 for figure 4) whereas the current–time trace of monopole-type self-oscillations should exhibit fewer current spikes [67]. Together with the evidence provided by photoluminescence measurements, the current–time traces in figure 4(a) support the conclusion that self-sustained current oscillations for that SL at the bias conditions indicated are due to recycling and motion of monopole wavefronts.

3. Models

In weakly coupled SL, the main transport mechanism is sequential resonant tunnelling. Nonlinear phenomena seen in experiments can be described by discrete balance equations. Early models were motivated by static domain formation, and we may cite Likharev *et al* [47], Laikhtman [44] and Laikhtman and Miller [45] among the first authors who recognized the importance of using discrete equations. In this paper, I will describe a model of SL transport introduced in 1994 by our group [8], aspects of which have been steadily improved on in collaboration with other groups, particularly Platero's and Schöll's. Models of the same type (involving two electron populations corresponding to the lowest two subbands instead of just one electron density) were put forward by Schöll and his group, also starting in 1994 [63, 83].

3.1. Assumptions and the discrete drift-diffusion model

For a weakly coupled doped SL, there are certain important timescales that are well separated. The scattering time is the time that an electron originally in an excited subband takes to lose energy and fall to the first subband. The escape time or tunnelling time is the average time that an electron needs to escape from one well to the adjacent one. Finally, the dielectric relaxation time is the longer timescale over which the local electric field at a SL period evolves. The latter yields the order of magnitude of the period of self-sustained oscillations, and it is of the order of the SL length divided by an average electron velocity. In a weakly coupled SL, the scattering time is much smaller than the tunnelling time, and the latter is much smaller than the macroscopic dielectric relaxation time. Then the dominant mechanism of vertical transport is sequential tunnelling; only the first subband of each well is appreciably occupied, and the tunnelling current is quasistationary. The latter statement means that we can calculate the well-to-well tunnelling current density across a barrier assuming a constant value of the applied electric field and a constant electron density at the wells adjacent to the barrier. The resulting expression is then considered as the *constitutive relation* between the tunnelling current and the local electric field(s) and electron densities at the wells adjacent to the barrier.

We count the barrier separating the injecting contact from the first well of the SL as the zeroth barrier. Then the ith SL period starts on the right of the $(i-1)$th barrier and ends on the right of the ith barrier. Barriers and wells have widths d and w, respectively, so $l = d + w$ is the SL period. With this convention, we will adopt, as dependent barriers of our model, *minus* the electric field averaged over the ith period, F_i, and the two-dimensional electron density at the ith well (concentrated in a plane normal to the growth direction, located at the end of the ith well), n_i. These variables obey the Poisson and charge continuity equations:

$$F_i - F_{i-1} = \frac{e}{\varepsilon}(n_i - N_D^w) \tag{3.1}$$

$$\frac{\mathrm{d}n_i}{\mathrm{d}t} = J_{i-1\to i} - J_{i\to i+1}. \tag{3.2}$$

Here N_D^w, ε, and $eJ_{i\to i+1}$ are the 2D doping density at the ith well, the average permittivity of the SL, and the tunnelling current density across the ith barrier, respectively. We can differentiate equation (3.1) with respect to time and eliminate n_i by using equation (3.2). The result can be written as a form of Ampère's law for the balance of current:

$$\frac{\varepsilon}{e}\frac{\mathrm{d}F_i}{\mathrm{d}t} + J_{i\to i+1} = J(t). \tag{3.3}$$

Here $eJ(t)$ is the total current density through the SL, equal for all SL periods, and $\varepsilon\,\mathrm{d}F_i/\mathrm{d}t$ is the displacement current at the ith SL period.

The tunnelling current density $eJ_{i\to i+1}$ is related to electric fields and electron densities by a *constitutive relation*, which could be fitted to available experimental data or, more desirably, derived from first principles. At present, there are two such derivations, none of which is completely satisfactory. Both derivations assume the separation between relevant timescales explained above and calculate a quasistationary tunnelling current density. The first derivation is based upon calculating the tunnelling current by the transfer Hamiltonian method (THM). It is assumed that the barriers are sufficiently thick that different wells are weakly coupled, and that the voltage drops at barriers and wells are uniform in space. This method leads to a more detailed discrete model [1] which resolves the fast timescale corresponding to current spikes even at second and higher plateaus [67]. It yields the tunnelling current and boundary conditions in a natural way. The second derivation uses the method of nonequilibrium Green functions (in a Wannier basis) for an infinite SL which is subject to a constant electric field and is in a stationary spatially homogeneous state [82, 83]. In principle, an approach from this point of view could lead to derivation of more general discrete models of hydrodynamic type, or to consideration of the transition between weakly and strongly coupled SL, although these desirable goals have not been achieved so far.

If we assume that the potential drops at barriers and wells are proportional to an average field F_i (at the ith SL period), either THM or stationary Green function calculations yield expressions for the tunnelling current of the form $J_{i\to i+1} = \mathcal{J}(n_i, n_{i+1}, F_i; T)$. Here T is the lattice temperature, which is supposed to be the same as the electron temperature. This ignores hot-carrier effects and it is not correct in general. Somewhat more general models with an average electron temperature T_i at the ith SL period have been proposed, including a phenomenological equation for the temperature [77]. A general derivation of the balance equations (including the equation for the temperature) would clarify these issues. For sufficiently high temperatures (see appendix A), we can adopt the following drift-diffusion form for the constitutive relation [12]:

$$J_{i\to i+1} = \frac{n_i v(F_i)}{l} - D(F_i)\frac{n_{i+1} - n_i}{l^2}, \tag{3.4}$$

where the *drift* velocity is an odd function of the field, $v(-F) = -v(F)$, and the *diffusion coefficient* satisfies the relation

$$D(-F) = v(F)l + D(F). \tag{3.5}$$

These coefficients can be calculated from the formulae

$$v(F) = \frac{l\mathcal{J}(N_D^w, N_D^w, F; T)}{N_D^w},$$

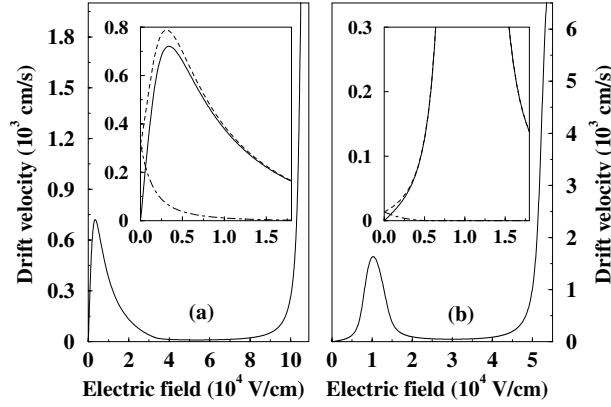$$D(F) = -\frac{l^2\mathcal{J}(0, N_D^w, F; T)}{N_D^w}. \tag{3.6}$$

Figure 5. (*a*) The calculated electron drift velocity $v(F)$ for the 9/4 SL at 0 K. Inset: comparison of the drift velocity $v(F)$ (continuous curve) with the forward $v^{(f)}(F) = v(F) + D(F)/l$ (dashed curve) and backward $v^{(b)}(F) = D(F)/l$ (dot–dashed curve) velocities. (*b*) The same, but for the 13.3/2.7 SL. Notice that the backward velocity, or equivalently the diffusivity, decreases with electric field much more rapidly for this SL (reprinted from [12]).

Typical forms are shown in figure 5. Analytical formulae for the tunnelling current and these coefficients can be explicitly derived in the limit of narrow scattering widths; see appendix A. The Ampère law corresponding to the current in equation (3.4) is

$$\frac{\varepsilon}{e}\frac{\mathrm{d}F_i}{\mathrm{d}t} + \frac{n_i v(F_i)}{l} - D(F_i)\frac{n_{i+1} - n_i}{l^2} = J(t). \tag{3.7}$$

Equations (3.1) and (3.7) form the discrete DDD, which we will study in the rest of this article. Notice that for high fields (in practice for all plateaus except the first one), $D = 0$, and we have a simpler discrete drift model [8,9] with $J_{i\to i+1} = n_i v(F_i)/l$.

The boundary conditions for the contact regions at the ends of the SL should be equation (3.3) at $i = 0$ and N, with appropriate constitutive relations for the tunnelling current across the 0th and Nth barriers. A derivation from the THM yields the following expressions:

$$J_{0\to 1} = j_e^{(f)}(F_0) - \frac{n_1}{l}w^{(b)}(F_0), \tag{3.8}$$

$$J_{N\to N+1} = \frac{n_N}{l}w^{(f)}(F_N), \tag{3.9}$$

where $j_e^{(f)}$, $w^{(b)}$, and $w^{(f)}$ are functions of the local field. Coefficient functions corresponding to the 9/4 sample of [40] are represented in figure 6. They have shapes that are typical for similar SL. Let us emphasize here that many other boundary conditions have been used in the literature, mostly introduced in a phenomenological manner. Among them, let us quote, using Ohm's law for the injecting contact, $j_e^{(f)} = \sigma F_0$, $w^{(b)} = 0$, and a linear velocity function at the collector, $w^{(f)} = \sigma l F_N/N_D^w$; see [3], and section 5 below. Selecting the contact conductivity σ_e appropriately, it is then possible to obtain both monopole wavefronts and charge dipole domains (pulses of the electric field). Calculations with the discrete drift model typically use $n_1 = (1 + c)N_D^w$, which phenomenologically accounts for an excess of electrons in the first well of the SL coming from the emitter region. This boundary condition results in self-sustained current oscillations due to monopole recycling if $c > 0$ [10, 15, 34, 40]. Notice that the discrete drift model has zero diffusivity, so we only need one boundary condition, for $F_0 = F_1 - e(n_1 - N_D^w)/\varepsilon$.
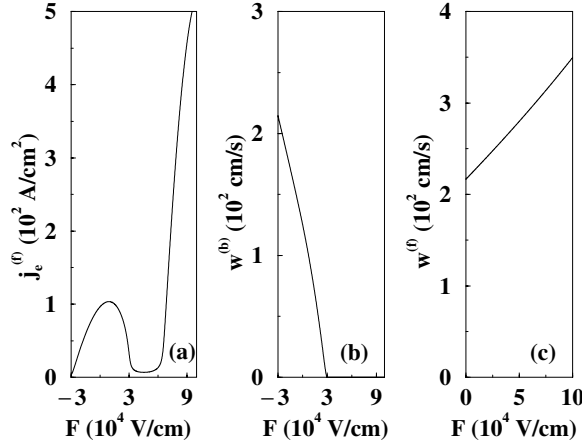
Figure 6. Functions of the electric field appearing in the boundary conditions for the 9/4 SL with a contact doping $N_D = 2 \times 10^{18}$ cm^{-3}. (a) $ej_e^{(f)}(F)$ and (b) $w^{(b)}(F)$ for the emitter, and (c) $w^{(f)}(F)$ for the collector (reprinted from [12]).

Lastly, we need a bias condition to completely specify our DDD model. Most experiments are carried out under voltage bias conditions, which means that $V(t)$ in

$$\frac{1}{N} \sum_{i=1}^{N} F_i = \frac{V(t)}{Nl} \tag{3.10}$$

is a known function.

To analyse the discrete DDD, it is convenient to render all equations dimensionless. Let $v(F)$ reach its first positive maximum at (F_M, v_M). We adopt F_M, N_D^w, v_M, $v_M l$, $eN_D^w v_M/l$, and $\varepsilon F_M l/(eN_D^w v_M)$ as the units of F_i, n_i, $v(F)$, $D(F)$, eJ, and t, respectively. For the first plateau of the 9/4 SL of [40], we find $F_M = 6.92$ kV cm^{-1}, $N_D^w = 1.5 \times 10^{11}$ cm^{-2}, $v_M = 156$ cm s^{-1}, $v_M l = 2.03 \times 10^{-4}$ cm^2 s^{-1}, and $eN_D^w v_M/l = 2.88$ A cm^{-2}. For a circular sample with a diameter of 120 μm, the units of current and time are 0.326 mA and 2.76 ns, respectively. Then equations (3.1), (3.7), to (3.10) become

$$\frac{dE_i}{dt} + v(E_i)n_i - D(E_i)(n_{i+1} - n_i) = J, \tag{3.11}$$

$$E_i - E_{i-1} = \nu(n_i - 1), \tag{3.12}$$

$$\frac{1}{N} \sum_{i=1}^{N} E_i = \phi, \tag{3.13}$$

$$\frac{dE_0}{dt} + J_e(E_0) - w_e(E_0)n_1 = J, \tag{3.14}$$

$$\frac{dE_N}{dt} + w_c(E_N)n_N = J. \tag{3.15}$$

Here we have used the same symbols for dimensional and dimensionless quantities except for the electric field (F dimensional, E dimensionless). The parameters $\nu = eN_D^w/(\varepsilon F_M)$ and $\phi = V/(F_M Nl)$ are dimensionless doping and average electric field (bias), respectively. For the 9/4 SL, $\nu \approx 3$. We recall that $i = 1, \ldots, N-1$ in (3.11) and $i = 1, \ldots, N$ in (3.12). In equations (3.14) and (3.15), $J_e(E_0) = j_e^{(f)}(F_M E_0)l/(N_D^w v_M)$, $w_e(E_0) = w^{(b)}(F_M E_0)/v_M$, $w_c(E_N) = w^{(f)}(F_M E_N)/v_M$. As a handy reference, we give below a table with the definitions

Table 1. Definitions of the units that we have used to nondimensionalize the model equations and their numerical values for the first plateau of the 9/4 SL.

F	n	v	D	eJ	t
F_M	N_D^w	v_M	$v_M l$	$\dfrac{eN_D^w v_M}{l}$	$\dfrac{\varepsilon F_M l}{eN_D^w v_M}$
6.92 kV cm^{-1}	$1.5 \times 10^{11} \text{ cm}^{-2}$	156 cm s^{-1}	$2.03 \times 10^{-4} \text{ cm}^2 \text{ s}^{-1}$	2.88 A cm^{-2}	2.76 ns

of the units that we have used to nondimensionalize the model equations and their numerical values for the first plateau of the 9/4 SL (table 1). Given a dimensionless magnitude we should multiply it by its corresponding unit in the table to obtain its value in physical units. In addition to the numerical values included in the table (corresponding to the first plateau of the 9/4 SL of [40]), we can calculate F_M, v_M, and so on for any SL or plateau in which we may be interested. Then we can use the corresponding numerical values to compute the units listed in the table, and translate the dimensionless values of the magnitudes given by the theory into physical dimensional units. Using dimensionless units has the following advantages:

 (i) redundant parameters in the equations are eliminated, and
(ii) different terms in the equations can be properly compared. Thus the task of neglecting small terms can be appropriately carried out.

4. Stationary states and wavefronts

4.1. Wavefronts on an infinite superlattice

Here we shall consider an infinite SL under constant current bias J described by equations (3.11) and (3.12), or equivalently,

$$\frac{\mathrm{d}E_i}{\mathrm{d}t} + v(E_i)\frac{E_i - E_{i-1}}{\nu} = D(E_i)\frac{E_{i+1} + E_{i-1} - 2E_i}{\nu} + J - v(E_i). \qquad (4.1)$$

Clearly, there are two stable spatially homogeneous stationary solutions, namely $E^{(1)}(J)$ and $E^{(3)}(J)$, where $v(E^{(k)}) = J$, $E^{(1)}(J) < E^{(2)}(J) < E^{(3)}(J)$. We are interested in nonuniform wavefront states of the DDD model which satisfy $E_i \to E^{(1)}(J)$ as $i \to -\infty$ and $E_i \to E^{(3)}(J)$ as $i \to \infty$. These states correspond to electron accumulation layers: $n_i - 1 = (E_i - E_{i-1})/\nu > 0$. It is also possible to have *electron depletion layers* such that $E_i \to E^{(3)}(J)$ as $i \to -\infty$ and $E_i \to E^{(1)}(J)$ as $i \to \infty$, with $n_i - 1 < 0$. Electron accumulation wavefront states are either stationary or time dependent. In the second case, they are wavefronts moving with constant velocity $c = c(J, \nu)$, such that $E_i(t) = E(i - ct)$, $i = 0, \pm 1, \ldots, E(\tau)$, is a smooth profile which solves the following nonlinear eigenvalue problem for c (measured in wells traversed per unit time) and $E(\tau)$:

$$c\frac{\mathrm{d}E}{\mathrm{d}\tau} = v(E) - J + v(E)\frac{E - E(\tau - 1)}{\nu} - D(E)\frac{E(\tau + 1) + E(\tau - 1) - 2E}{\nu}, \qquad (4.2)$$

$$E(-\infty) = E^{(1)}(J), \qquad E(\infty) = E^{(3)}(J). \qquad (4.3)$$

Electron depletion wavefronts obey the same equation with the obvious change in boundary conditions. No rigorous study of pinning of depletion wavefronts exists, although comparison methods [24] should work with them too. So far, numerical simulations have always shown depletion wavefronts moving with positive velocity. As we will see later, wavefronts are the key to understanding more complex phenomena related to the dynamics of electric field domains. From now to the end of this section, we shall consider electron accumulation

wavefronts only. By using a comparison principle, the existence of stationary fronts has been rigorously proved [24]. Outside the interval of current values in which there are stationary fronts, we can only prove that there are fronts moving to the right or the left [24]. Moving and stationary fronts cannot exist simultaneously at the same value of the current [25].

4.1.1. Pinning. Numerical simulations of (4.1) show that, after a short transient, a variety of initial conditions such that $E_i \to E^{(1)}(J)$ as $i \to -\infty$ and $E_i \to E^{(3)}(J)$ as $i \to \infty$ evolved towards either a stationary or moving monopole. For systematic numerical studies, we have therefore adopted an initial steplike profile, with $E_i = E^{(1)}(J)$ for $i < 0$, $E_i = E^{(3)}(J)$ for $i > 0$, and $E_0 = E^{(2)}(J)$. The boundary data are taken to be $E_{-N} = E^{(1)}(J)$, $E_N = E^{(3)}(J)$ with N large. Figure 7 is a phase diagram showing the regions in the plane (J, ν) where different wavefronts are stable. There are two important values of ν, $\nu_1 < \nu_2$. The critical value ν_1 defines the minimum doping value needed for a stationary monopole to exist, whereas ν_2 is the minimum doping needed for a monopole to move upstream with $c < 0$:

- For $0 < \nu < \nu_1$ and each fixed J in the interval $(\nu_m, 1)$, only travelling monopole fronts moving downstream (to the right) are observed. This implies that there will be no experimental observation of static current branches if the 2D doping obeys $N_D^w < \nu_1 \epsilon F_M / e$. For $\nu > \nu_1$, stationary monopoles are found (and static current branches in the SL I–V characteristic can be experimentally observed); see figure 7. The upper bounds for ν_1 are [24]

$$\nu_{1b}(J) = \nu_m \frac{E_m - E^{(1)}(J)}{1 - \nu_m}, \tag{4.4}$$

$$\nu_c = \min \nu_{1b}(J) = \nu_m \frac{E_m - 1}{1 - \nu_m}. \tag{4.5}$$

  The smallest possible bound $\nu_{1b}(J)$ is $\nu_c = 0.198$, for our numerical example. We have found that the smallest value of $\nu_1(J)$ is 0.16.

- For $\nu_1 < \nu < \nu_2$, travelling fronts moving downstream exist only if $\nu_m < J < J_1(\nu)$, where $J_1(\nu) < 1$ is a critical value of the current; see figure 7. If $J_1(\nu) < J < 1$, the stable solutions are steady fronts (stationary monopoles). We have found that $\nu_2 = 0.33$.

- New solutions are observed for $\nu > \nu_2$. As before, there are travelling fronts moving downstream if $\nu_m < J < J_1(\nu)$, and stationary monopoles if $J_1(\nu) < J < J_2(\nu)$, $J_2(\nu) < 1$ is a new critical current; see figure 7. For $J_2(\nu) < J < 1$, the stable solutions of (4.1) are monopoles travelling upstream (to the left). As ν increases, $J_1(\nu)$ and $J_2(\nu)$ approach ν_m and 1, respectively. Thus stationary solutions are found for most values of J if ν is large enough.

Figure 7 depicts $J_1(\nu)$ and $J_2(\nu)$ as functions of ν. The dashed lines are analytical expressions for $J_1(\nu)$ and $J_2(\nu)$ that are calculated by using a comparison principle and the numerical forms for $\nu(E)$ and $D(E)$, while the solid curves result from a full simulation of equation (4.1); see [24]. Notice that J_1 decreases from $J_1 = 1$ to ν_m as ν increases from ν_1. Similarly, J_2 decreases from $J_2 = 1$ to a minimum value $J_2 \approx 0.53$ and then increases back to $J_2 = 1$ as ν increases. Thus we see that the pinning interval (J_1, J_2) at which fronts are stationary is narrower for doping such that $J_2(\nu)$ reaches its minimum. For larger ν, the interval of J for which stationary solutions exist becomes wider again, getting closer to spanning the whole interval $(\nu_m, 1)$ as $\nu \to \infty$. For very large ν, the velocities of downstream and upstream moving monopoles become extremely small in absolute value.

Monopole velocity as a function of current has been depicted in figure 8 for the first plateau of the 9/4 SL in [40]. Notice that, for the DDD model, the interval of current values at which
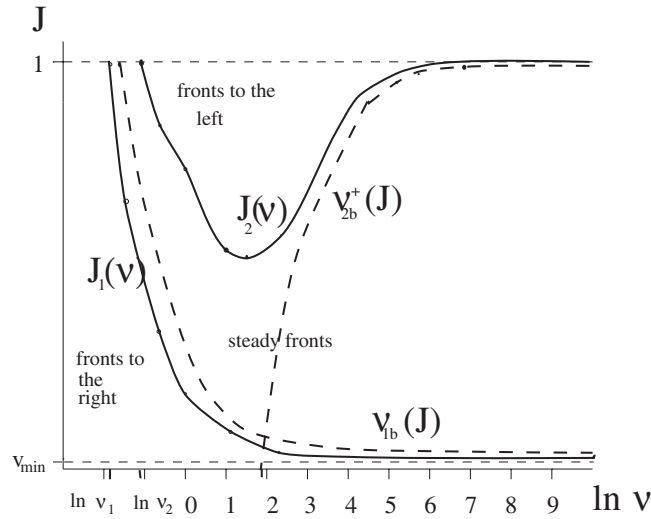
Figure 7. Critical currents J_1 and J_2 as functions of the dimensionless doping ν. Monopoles move downstream for $\nu_m < J < J_1(\nu)$, are stationary for $J_1(\nu) < J < J_2(\nu)$, and move upstream for $J_2(\nu) < J < 1$. Dashed curves in this figure represent theoretical bounds $\nu_{1b}(J)$ and $\nu_{2b}^+(J)$ derived in [24] (reprinted from [24]).
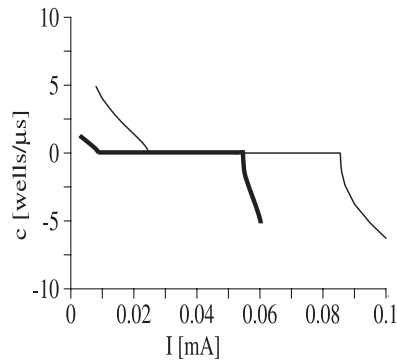

Figure 8. Velocity of a monopole wavefront as a function of the current for the first plateau of the 9/4 SL in [40]. Results for the discrete DDD with $\nu = 3$ (thick curve) have been compared to those obtained by using the exact tunnelling current $eJ_{i \to i+1} = e\mathcal{J}(n_i, n_{i+1}, F_i; T)$ (thin curve) instead of the approximation given by equation (3.4). Notice that both the DDD model and the model with the more general tunnelling current exhibit a pinning interval for the current at which $c = 0$, and current intervals for which the monopoles move upstream or downstream in the electron flux (reprinted from [24]).

wavefronts are stationary is shifted to lower values of the current with respect to the more general tunnelling current $e\mathcal{J}(n_i, n_{i+1}, F_i; T)$ given by the THM or Green function methods; see [24].

There are two limits in which analytical understanding of wavefront motion has been achieved: the continuum limit $\nu \to 0$ (with finite values of νN); and the strongly discrete limit of sufficiently large ν. The transition from moving to stationary wavefronts is best understood in the strongly discrete limit [26], while we have a theory of wavefront recycling in the continuum limit.
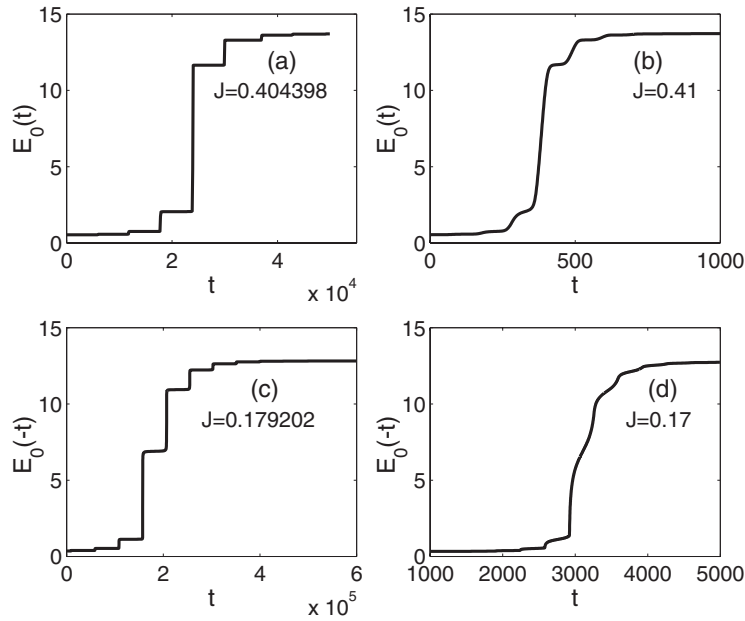
Figure 9. Sharpening of wavefront profiles as the dimensionless current J approaches its critical values for $\nu = 3$. (a) $J \approx J_2$, (b) $J > J_2$, (c) $J \approx J_1$, (d) $J < J_1$ (reprinted from [27]).

4.1.2. Pinning of wavefronts with a single active well. At the critical currents, $J_1(\nu)$ and $J_2(\nu)$, wavefronts moving downstream (to the right, following the electron flow, $c > 0$) for smaller J or upstream (to the left, against the electron flow, $c < 0$) for larger J fail to propagate. What happens is that the wavefront field profile $E(\tau)$ becomes sharper as J approaches the critical currents; see figure 9. Exactly at J_k, $k = 1, 2$, gaps open up in the wavefront profile which therefore loses continuity. The resulting field profile is a stationary front $E_i = E_i(J, \nu)$: the wavefront is pinned for $J_1 < J < J_2$. The depinning transition (from stationary fronts to moving wavefronts) is technically speaking a global saddle-node bifurcation. We shall study it first in the simplest case of large dimensionless doping ν, and then indicate what happens in the general case.

For sufficiently large doping and J close to a critical current (either J_1 or J_2), the moving front is led by the behaviour of a single well, which we will call the *active well*. If we examine the shape of a stationary front near the critical current, we observe that all wells are close either to $E^{(1)}(J)$ or $E^{(3)}(J)$ except for one well which drifts slowly and eventually jumps: the active well. Let us call E_0 the electric field at the active well. Since all wells in the front perform the same motion, we can reconstruct the profile $E(i - ct)$ from the time evolution of $E_0(t) = E(-ct)$. Before the active well jumps, $E_i \approx E^{(1)}(J)$ for $i < 0$ and $E_i \approx E^{(3)}(J)$ for $i > 0$. Thus equation (3.10) becomes

$$\frac{dE_0}{dt} \approx J - v(E_0) - v(E_0)\frac{E_0 - E^{(1)}}{\nu} + D(E_0)\frac{E^{(1)} + E^{(3)} - 2E_0}{\nu}. \qquad (4.6)$$

This equation has three stationary solutions for $J_1 < J < J_2$, two stable and one unstable, and only one stable stationary solution otherwise. At the critical currents, two of these solutions coalesce forming a saddle node. At low values of the current, the two coalescing solutions are a double zero (multiplicity two) of the right-hand side of equation (4.6) corresponding to a local maximum thereof. For high currents, the two coalescing solutions are a double zero of

the right-hand side of equation (4.6) corresponding to a local minimum thereof. The critical currents are such that the expansion of the right-hand side of (4.6) about the two coalescing stationary solutions,

$$J - v(E_0) - v(E_0)\frac{E_0 - E^{(1)}}{\nu} + D(E_0)\frac{E^{(1)} + E^{(3)} - 2E_0}{\nu} = 0, \qquad (4.7)$$

has zero linear term,

$$D_0'(E^{(1)} + E^{(3)} - 2E_0) - 2D_0 - v_0'(E_0 - E^{(1)}) - v_0 - \nu v_0' = 0. \qquad (4.8)$$

Here D_0' means $D'(E_0) = (\mathrm{d}D/\mathrm{d}E)(E_0)$, etc. Equations (4.7) and (4.8) yield approximations to E_0 and the critical current J_c (which is either J_1 or J_2). The results show excellent agreement with those of numerical solutions of the model for $\nu > 2$. Our approximation performs less well for smaller ν, which indicates that more active wells are needed to improve it.

Let us now construct the profile of the travelling wavefronts after depinning, for J slightly below J_1 or slightly above J_2. We shall use the method of matched asymptotic expansions [6]. The idea is to describe the jump of an active well from $E^{(1)}(J)$ to $E^{(3)}(J)$ if $J > J_2$ (or from $E^{(3)}(J)$ to $E^{(1)}(J)$ if $J < J_1$) by means of two separate stages. During the first stage, $E_0(t)$ stays very close to its stationary value at the critical current, $E_0(J_c)$, for a very long time. After reaching a certain blow-up time, the active well jumps to $E^{(3)}(J)$ (or it falls to $E^{(1)}(J)$) on a faster timescale, as suggested by the numerical results depicted in figures 9(a) and (c). The process is then repeated until the active well reaches either $E^{(3)}(J)$ or $E^{(1)}(J)$. Let us start with the slow stage. Up to terms of order $|J - J_c|$, equation (4.6) becomes

$$\frac{\mathrm{d}\varphi}{\mathrm{d}t} \approx \alpha(J - J_c) + \beta\varphi^2, \qquad (4.9)$$

for $E_0(t) = E_0(J_c) + \varphi(t)$, as $J \to J_c$. $E_0(J_c)$ is the stationary solution of (4.6) at $J = J_c$. The coefficients α and β are given by

$$\alpha = 1 + \frac{v_0 + D_0}{\nu v_1'} + \frac{D_0}{\nu v_3'}, \qquad (4.10)$$

$$2\nu\beta = D_0''(E^{(1)} + E^{(3)} - 2E_0) - 4D_0' - 2v_0' + v_0''(E^{(1)} - E_0 - 2\nu). \qquad (4.11)$$

β is negative if $J_c = J_1$ and positive if $J_c = J_2$. Equation (4.9) yields the outer approximation to the depinning transition [6], and it has the solution

$$\varphi(t) \sim (-1)^k \sqrt{\frac{\alpha(J - J_k)}{\beta}} \tan\left(\sqrt{\alpha\beta(J - J_k)}(t - t_0)\right) \qquad (4.12)$$

$(k = 1, 2)$, for J such that $\mathrm{sgn}(J - J_k) = \mathrm{sgn}\,\beta$. The amplitude (4.12) is very small most of the time, but it blows up when the argument of the tangent function approaches $\pm\pi/2$. Thus the outer approximation holds over a time interval $(t - t_0) \sim \pi/\sqrt{\alpha\beta(J - J_k)}$. The reciprocal of this time interval yields an approximation for the wavefront velocity:

$$|c(J, \nu)| \sim \frac{\sqrt{\alpha\beta(J - J_k)}}{\pi}. \qquad (4.13)$$

In figures 10 and 11, we compare this approximation with the numerically computed velocity for $\nu = 3$ and 20, respectively. The agreement is excellent. Notice that for the smaller value, $\nu = 3$, we need to improve our approximations considering that there are several *active wells*, $E_{-L}(t), \ldots, E_0(t), \ldots, E_M(t)$, that differ from either $E^{(1)}(J)$ or $E^{(3)}(J)$ during the wavefront motion: $E_{-i} = E^{(1)}(J)$ if $i > L$ and $E_i = E^{(3)}(J)$ if $i > M$. The corresponding theory is similar to the one we have described except that we consider a system of finitely many differential equations (for the active wells) instead of the single equation (4.6) [27].
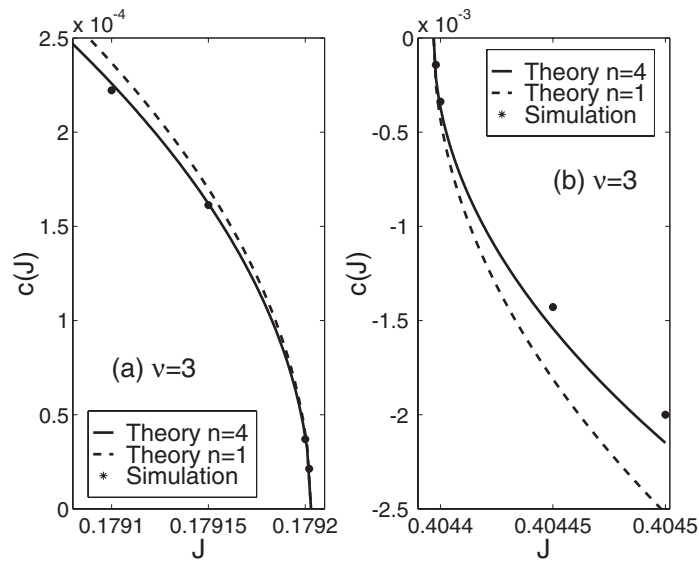
Figure 10. Wavefront velocity as a function of current density for $\nu = 3$. We have compared the numerically measured velocity to the results from our theory with one or four active wells (reprinted from [27]).
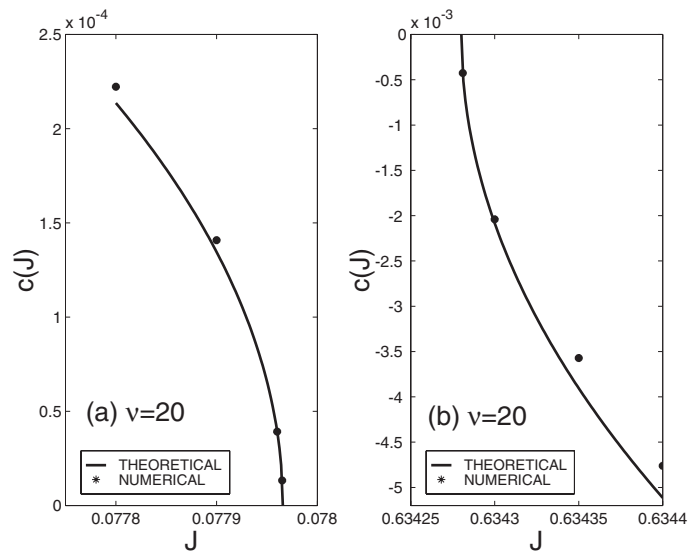
Figure 11. Wavefront velocity as a function of current density for $\nu = 20$. We have compared the numerically measured velocity to the results from our theory with one active well (reprinted from [27]).

When the solution begins to blow up, the outer solution (4.12) is no longer a good approximation, for $E_0(t)$ departs from the stationary value $E_0(J_c)$. We must go back to (4.6) and obtain an inner approximation to this equation [6]. As J is close to J_c and $E_0(t) - E_0(J_c)$ is of order 1, we solve (4.6) numerically at $J = J_c$ with the matching condition that
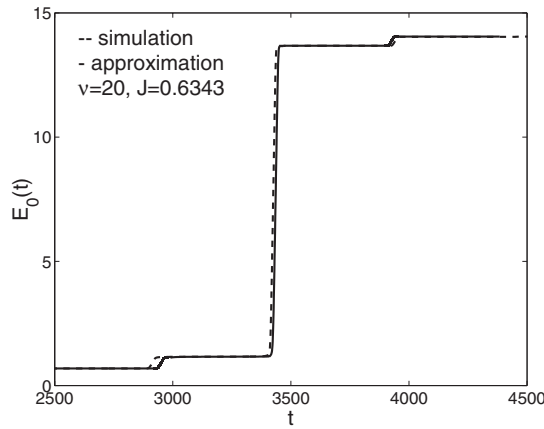
Figure 12. Wavefront profiles near $J = J_2$ for $\nu = 20$. The results of matched asymptotic expansions with one active well and the numerical solution of the model are compared (reprinted from [27]).

$E_0(t) - E_0(J_c) \sim (-1)^k 2/[\pi \sqrt{\beta/[\alpha(J - J_c)]} - 2|\beta|(t - t_0)]$, as $(t - t_0) \to -\infty$. This inner solution describes the jump of E_0 to values close to $E^{(1)}$ if $J_c = J_1$, or to values close to $E^{(3)}$ if $J_c = J_2$. During this jump, the motion of E_0 forces the other points to move. Thus, for $J_c = J_1$, $E_1(t)$ can be calculated by using the inner solution in (4.1) for E_0, with $J = J_c$ and $E_2 \approx E^{(3)}$. Similarly, for $J_c = J_2$, $E_{-1}(t)$ can be calculated by using the inner solution in (4.1) for E_0, with $J = J_c$ and $E_{-2} \approx E^{(1)}$. A composite expansion [6,7] constructed with these inner and outer solutions is compared to the numerical solution of the model in figure 12. Notice that we can reconstruct the travelling wave profiles $E(i - ct)$ from the identity $E_0(t) = E(-ct)$ by rescaling the horizontal axis in figure 12.

4.1.3. Continuum limit. The continuum limit of the DDD model is useful for understanding self-sustained oscillations of the current and wavefront motion [9]. It consists of $\nu \to 0$, $i \to \infty$, with $\nu i = x \in [0, N\nu]$, $N\nu \gg 1$. In this limit, equations (3.11) and (3.12) yield

$$\frac{\partial E}{\partial t} + v(E)\frac{\partial E}{\partial x} = J - v(E), \tag{4.14}$$

up to terms of order ν. Equation (4.14) corresponds to the hyperbolic limit of the well-known Kroemer model of the Gunn effect [36]. Notice that a wavefront joining $E^{(1)}(J)$ to $E^{(3)}(J)$ with $\partial E/\partial x > 0$ (or with $\partial E/\partial x < 0$) and zero velocity cannot exist because $J - v(E)$ in equation (4.14) changes sign at $E = E^{(2)}(J)$. Thus wavefronts cannot be pinned in the continuum limit. As we show now, wavefronts can be constructed by using shock waves (i.e., moving discontinuous electric field profiles). With constant J, shock waves are solutions of these equations and their speed can be calculated explicitly [43,56]. Let $V(E_+, E_-)$ denote the speed of a shock wave such that E becomes E_- (or E_+) to the left (or right) of the shock wave. Inside the shock wave, we should use the discrete model. The wavefront velocity should be rescaled such that $V = c\nu$ is the correct velocity for the (rescaled) continuum profile $E(x - Vt) = E(\nu(i - ct)) = E_i(t)$. Let $E'(\xi) = dE/d\xi$ and $\dot{E}_i(t) = dE_i/dt$ with $\xi = x - Vt$. Then $E_i - E_{i-1} = E(\xi) - E(\xi - \nu) = \nu E'(\xi - \nu_0)$ with $0 < \nu_0 < \nu$ by the mean-value theorem. But we have $-VE'(\xi - \nu_0) = \dot{E}_i(t + \nu_0/V) = \dot{E}_i(t) + O(\nu)$, and, therefore, $dE_i/dt \sim -V(E_i - E_{i-1})/\nu$. Then

$$E_+ - E_- = \sum (E_i - E_{i-1}) = \nu \sum (n_i - 1)$$

$$\sim V \sum \frac{E_i - E_{i-1}}{v(E_i) + D(E_i)} + \sum \frac{D(E_i)}{v(E_i) + D(E_i)} \nu n_{i+1}$$

$$+ \nu \sum \left(\frac{J}{v(E_i) + D(E_i)} - 1 \right)$$

$$= V \sum \frac{E_i - E_{i-1}}{v(E_i) + D(E_i)}$$

$$+ \sum \frac{D(E_i)(E_{i+1} - E_i)}{v(E_i) + D(E_i)} + \nu \sum \left(\frac{J + D(E_i)}{v(E_i) + D(E_i)} - 1 \right).$$

This expression yields

$$V \sim \frac{\sum \frac{v(E_i)(E_{i+1} - E_i)}{v(E_i) + D(E_i)} - \nu \sum \frac{J - v(E_i)}{v(E_i) + D(E_i)}}{\sum \frac{E_i - E_{i-1}}{v(E_i) + D(E_i)}}.$$

Its numerator contains a term multiplied by ν which is bounded ($J = v(E_i)$ outside the wavefront) and vanishes in the continuum limit. Approximating Riemann sums by integrals in the remaining formula, the result is

$$V(E_+, E_-) = \frac{\int_{E_-}^{E_+} \frac{v(E)}{v(E) + D(E)} \, dE}{\int_{E_-}^{E_+} \frac{dE}{v(E) + D(E)}}, \tag{4.15}$$

or, equivalently, the following weighted equal-area rule:

$$\int_{E_-}^{E_+} \frac{v(E) - V(E_+, E_-)}{v(E) + D(E)} dE = 0. \tag{4.16}$$

For $D = 0$, this formula reduces to that derived for the discrete drift model in [9]. This formula can be corrected by using the trapezoid rule to evaluate integrals; see [27]. There is only one value of J, J^*, such that $V = J$ with $E_- = E^{(1)}(J)$ and $E_+ = E^{(3)}(J)$. For $J \in (v_m, J^*)$, a wavefront joining $E^{(1)}(J)$ to $E^{(3)}(J)$ consists of a shock wave having $E_+ = E^{(3)}(J)$, and E_- such that $V(E^{(3)}(J), E_-) = v(E_-)$. Furthermore, to the left of the shock wave, there is a *tail* region moving rigidly with the shock wave and such that

$$[v(E) - V] \frac{\partial E}{\partial \xi} = J - v(E), \tag{4.17}$$

for negative $\xi = x - Vt$, and $E(-\infty) = E^{(1)}(J)$, $E(0) = E_-$. This whole structure (shock wave and tail region) is called a *monopole with left tail* [10]. Similarly, for $J \in (J^*, 1)$, a wavefront joining $E^{(1)}(J)$ to $E^{(3)}(J)$ becomes a *monopole with right tail*. This monopole consists of a shock wave having $E_- = E^{(1)}(J)$, and E_+ such that $V(E_+, E^{(1)}(J)) = v(E_+)$, and a tail region satisfying (4.17) for positive ξ, with the boundary conditions $E(0) = E_+$ and $E(\infty) = E^{(3)}(J)$ [10]. In conclusion, the wavefront velocity as a function of J is determined by the following equations:

$$\begin{aligned} C(J) &= V(E^{(3)}(J), E_-), &&\text{with} \\ v(E_-) &= V(E^{(3)}(J), E_-), &&\text{if } v_m < J < J^*, \end{aligned} \tag{4.18}$$

$$\begin{aligned} C(J) &= V(E_+, E^{(1)}(J)), &&\text{with} \\ v(E_+) &= V(E_+, E^{(1)}(J)), &&\text{if } J^* < J < 1. \end{aligned} \tag{4.19}$$

We have compared the continuum approximation of the wavefront velocity (in wells traversed per unit time, i.e., $c(J, \nu) = C(J)/\nu$, not rescaled) with the numerical solution of the model for $\nu = 0.01$ in figure 13. The equal-area-rule result corresponds to (4.15), (4.18), and (4.19)
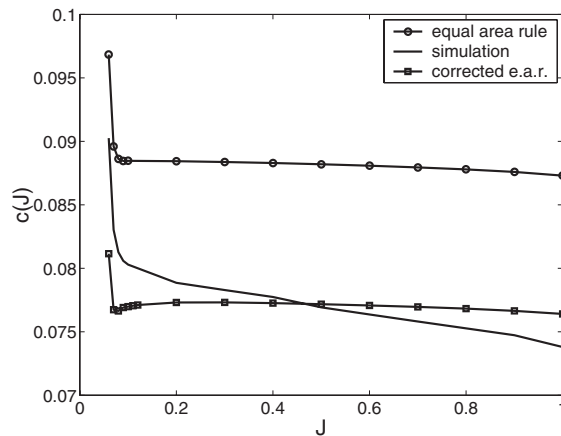
Figure 13. Comparison of the equal-area-rule (leading order) and corrected-equal-area-rule (including first-order corrections) approximations to the wavefront velocity with the numerical solution of the model for $\nu = 0.01$ (reprinted from [27]).

and its maximum difference from the numerical solution is about 17.6%. This result can be significantly improved if the integrals in (4.15) are approximated by the trapezoidal rule. Then the corrected equal-area result differs by at most 3% from the numerical solution [27].

4.1.4. Role of diffusivity. Discrete diffusivity or, more generally, back-tunnelling as in the term proportional to n_{i+1} in the tunnelling current of equation (A.8), is responsible for upstream-moving monopoles existing [24]. Thus for field values corresponding to the second and higher plateaus in the $I-V$ diagram, monopoles can only move downstream, because the diffusivity vanishes at high fields. For large doping, the active well $E_0(t)$ takes on a large-field value if J is close to the low value J_1, and it takes on a low-field value if J is close to the large value J_2. We could ignore diffusivity in certain expressions in our active well theory corresponding to the first case (monopoles moving downstream with $c > 0$), and still obtain reasonable numerical approximations for large enough doping values. If the dimensionless doping ν is small enough, monopoles can only move downstream with $c > 0$. In this case, the active well theory yields worse approximations and we can use the continuum limit theory in which diffusivity plays a minor role (it corrects the expression for monopole velocity).

4.2. Stationary states on a finite superlattice

Once different stable monopole solutions (moving either downstream or upstream, or stationary) have been identified, we raise the natural question of whether they are compatible with the boundary conditions. Numerical simulations at constant current show that the emitter boundary condition results in the creation of a charge accumulation (or depletion) layer near this contact. A charge depletion layer is formed near the collector contact as a result of the corresponding boundary condition. Except for these layers, the existence and configuration of monopoles moving downstream or upstream, or remaining stationary, agree with simulations corresponding to an infinitely long current-biased SL with a monopole-like initial condition. Thus stationary states on a finite SL are basically the stationary monopoles of the infinite SL but with their domain wall centred in one of the existing finitely many SL wells. When their corresponding $I-V$ diagram is produced, we obtain a characteristic curve similar to

that of figure 1(a) but with more regular looking branches: irregularity is due to doping fluctuations [71, 72, 82]. In this curve, the electric field profile of the nth branch (counted from left to right) has its domain wall located at the $N - n$ SL period (counted from the emitter).

For a finite voltage-biased SL, stationary solutions of the DDD model have to be found numerically. If we bias the SL on the second plateau of the I–V characteristic or above, $D \equiv 0$ and we can use the discrete drift model. Then stationary states can be obtained almost analytically [8, 9, 81]. The idea is that (4.1) becomes $E_{i-1} = E_i + [1 - J/v(E_i)]/\nu$, which corresponds simply to a one-dimensional discrete mapping. We need to solve this equation for E_i, $i = 1, \ldots, N$, with a boundary condition for E_0. Then the bias condition (3.13) can be used to determine J. The boundary condition $E_1 - E_0 = \nu c$, with positive c (physical meaning: there is an excess of electrons in the first SL well due to the emitter which results in a charge accumulation layer near it), has been widely used [9, 55, 81]. The 1D discrete mapping can be solved graphically together with the boundary condition for a fixed value of the current J. Then the average field $\Phi(J) = \sum_{i=1}^{N} E_i/N$ can be calculated and we can solve the equation $\Phi(J) = \phi$ graphically. This procedure has been carried out in [81]. Although it is rather immediate, no one has repeated these calculations with the theoretically better grounded boundary condition given by equation (3.14).

5. Relocation of electric field domains

In 1998, Luo *et al* [49] published experimental data on how a domain wall (belonging to a stable stationary electric field profile with two domains) relocates if the voltage across the SL is suddenly changed. These experiments have been explained recently by numerically simulating a discrete model with the tunnelling current given by equation (A.8) in appendix A [3]. New experiments have further confirmed the theory [65]. Let us now report in some detail the numerical simulations of [3] giving them a somewhat more elaborate theoretical interpretation. For the sake of simplicity, the contact functions in equations (3.8) and (3.9) will be selected as $ej_e^{(f)} = \sigma F_0$, $w^{(b)} = 0$, and $ew^{(f)} = \sigma F_N l/N_D^w$. Then

$$
\begin{aligned}
eJ_{0 \to 1} &= \sigma F_0, \\
eJ_{N \to N+1} &= \sigma F_N \frac{n_N}{N_D^w}.
\end{aligned}
\tag{5.1}
$$

The contact conductivity σ is selected such that charge dipole waves may propagate, which also occurs with (3.8) depending on the contact doping [12]. The factor n_N/N_D^w in the expression for $J_{N \to N+1}$ avoids negative electron densities at the collector. We simulate numerically a 40-well SL with barrier width $d = 4.0$ nm, well width $w = 9.0$ nm, doping $N_D^w = 1.5 \times 10^{11}$ cm^{-2}, $\gamma_{Ci} = 8$ meV (independent of the miniband index μ), and cross section $A = 15\,000$ μm^2, at a temperature $T = 5$ K. The parameters are those of the SL in [49]. Reasonable agreement with the overall shape of the experimental I–V characteristics in [49] is found if we adopt $\sigma = 0.01$ $(\Omega\,$m$)^{-1}$.

For the homogeneous case, i.e. $n_i = n_{i+1}$, the current density (A.8) depends on the electric field as in the typical N-shaped curve. The corresponding stationary I–V characteristic for inhomogeneous solutions is the typical sawtooth pattern of figure 14 with upper and lower branches corresponding to the up-sweep and down-sweep of the external voltage, respectively.

We show here the SL response to voltage switching starting from a point on the upper branch of the first plateau of the I–V characteristic at $V_{dc} = 0.75$ V (figure 14). After switching to a final voltage $V_f = V_{dc} + V_{step}$, the current will evolve towards a value on the stationary I–V characteristic corresponding to one of the branches at voltage V_f (in general there are several such branches due to multistability). We find that the final stationary current is on the
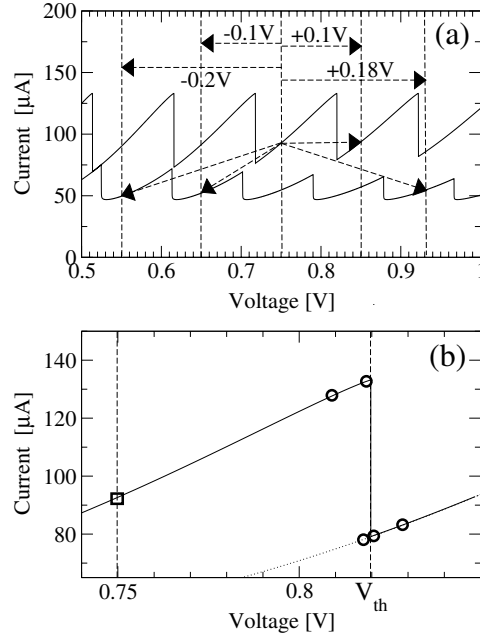
Figure 14. The simulated sawtooth I–V characteristic of a 40-well SL (4.0 nm AlAs barriers, 9.0 nm GaAs wells). Upper branches correspond to voltage up-sweep, lower branches to down-sweep. The arrows in (*a*) indicate the starting and end points of the voltage steps discussed in the text. (*b*) gives an enlarged view of the initial operating point (box) as well as of the different final points (circles) considered (reprinted from [3]).

upper branch if $V_{step} = 0.1$ V, while it is on the lower branch if $V_{step} = 0.18$ V; see the arrows in figure 14(*a*). Thus fast switching allows us to reach the lower branch by just increasing the voltage sufficiently. This is a striking result: in the conventional up-sweep and down-sweep, the point on the lower branch at 0.93 V can only be reached by increasing the voltage to more than 1.1 V and then decreasing to 0.93 V.

In figure 15(*a*), we depict the current response to different positive values of V_{step} versus time. For

$$V_{step} < V_{crit}, \tag{5.2}$$

with $V_{crit} \approx 0.175$ V, the current relaxes monotonically to its final value. There is a fundamentally different current response if equation (5.2) does not hold. Instead of relaxing monotonically, the current first drops to a level well below the lower stationary branch. Then the current response exhibits a fast repetitive double-peak pattern up to about 3 μs. Subsequently, following one larger spike, only single peaks occur. The spiky structure ends about 7 μs after the voltage switch, and the current evolves to a stationary value on the lower branch. The total number of peaks is roughly equal to the number of wells in the SL. The frequency of the peak burst is about 15 MHz. This behaviour does not change significantly as long as equation (5.2) is violated, even for very different values of V_{step}. This effect is very similar to the experimental observations in [49]. The quantitative difference is that the experimental total relaxation time is only about 2 μs. Such values could be achieved numerically, by choosing a larger scattering width $\gamma_{Ci} \approx 20$ meV.

How do we explain this behaviour? Let us use dimensionless units as follows. Consider the tunnelling current density of equation (A.8), $eJ_{i \to i+1} = e\mathcal{J}(n_i, n_{i+1}, F_i; T)$ evaluated
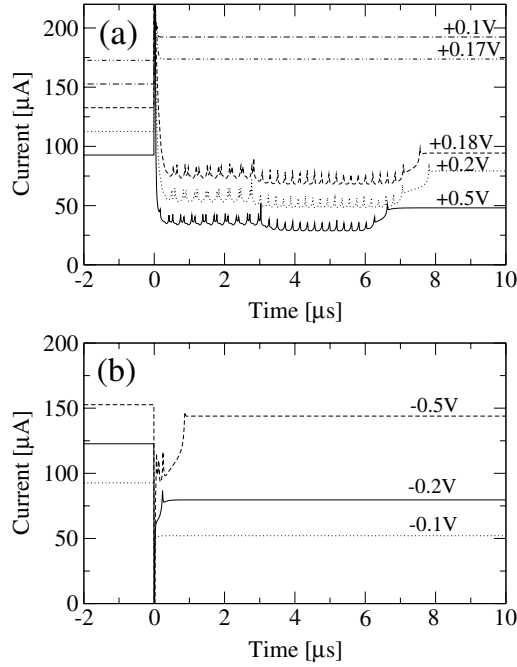
Figure 15. Current response versus time for various (*a*) positive and (*b*) negative voltage steps at $t = 0$. For $t < 0$, the voltage is $V_i = 0.75$ V. The curves are shifted vertically in units of 20 μA in (*a*) and 30 μA in (*b*) for clarity (reprinted from [3]).

at $n_i = n_{i+1} = N_D^w$ for a fixed $F_i = F$ and T. This curve is N-shaped, similar to the drift velocity $v(F)$. It has a local maximum at $F = F_M$ and eJ_M, and we can define $v_M = J_M l/N_D^w$. Let us define dimensionless units as in section 3 with these values, so that we have $v(E) = \mathcal{J}(N_D^w, N_D^w, F_M E; T)l/(N_D^w v_M)$. Furthermore, let us define $E^{(1)}(J)$, $E^{(2)}(J)$, and $E^{(3)}(J)$ to be the solutions of $v(E) = J$, ordered from smaller-field to higher-field values.

As in section 4, there are accumulation wavefronts joining $E^{(1)}(J)$ to $E^{(3)}(J)$ that have monotonically increasing field profiles with $E_i < E_{i+1}$; they move with velocities $c_+(J)$, which may be positive, zero, or negative; compare with figure 8. Furthermore, there are depletion wavefronts joining $E^{(3)}(J)$ to $E^{(1)}(J)$ that have monotonically decreasing wave profiles $E_i > E_{i+1}$. These wavefronts with a decreasing field profile have not been considered until now. They always move with positive velocities (no matter what positive value of J we take), which we shall denote by $c_-(J)$. The dimensionless velocities $c_+(J)$ and $c_-(J)$ are calculated with the full sequential tunnelling current (A.8) instead of using the DDD model as in section 4, and the result is depicted in figure 16. Approximations to $c_+(J)$ can be obtained from the active well theory for J close to J_1 or J_2, or even from the continuum limit $\nu \to 0$ (provided that the doping ν is not large). In the latter case, $c_-(J) \approx J$ (corresponding to $n \approx 0$ at the leading edge of a pulse) and the possibility $c_+ \leqslant 0$ is lost. The latter fact shows that the continuum limit may be a poor approximation of wavefront dynamics if the current is large enough, unless the doping is sufficiently low.

As explained before, electron accumulation monopoles may have positive, zero, or negative velocities, as the current is increased. The current interval (I_l, I_u), corresponding to stationary monopoles, depends on the location and size of the peak and bottom values of the sequential tunnelling current equation (A.8). For the DDD model, $I_l = eN_D^w v_M J_1/l$,
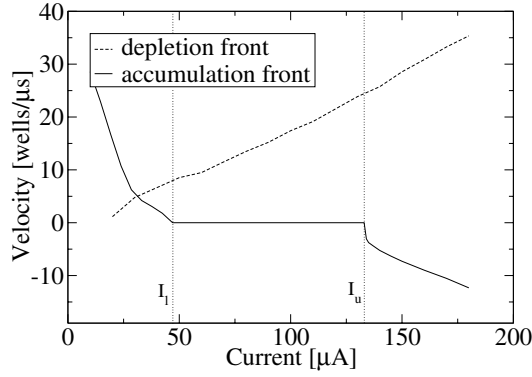
Figure 16. Front velocity versus current for electron depletion and accumulation fronts (reprinted from [3]).
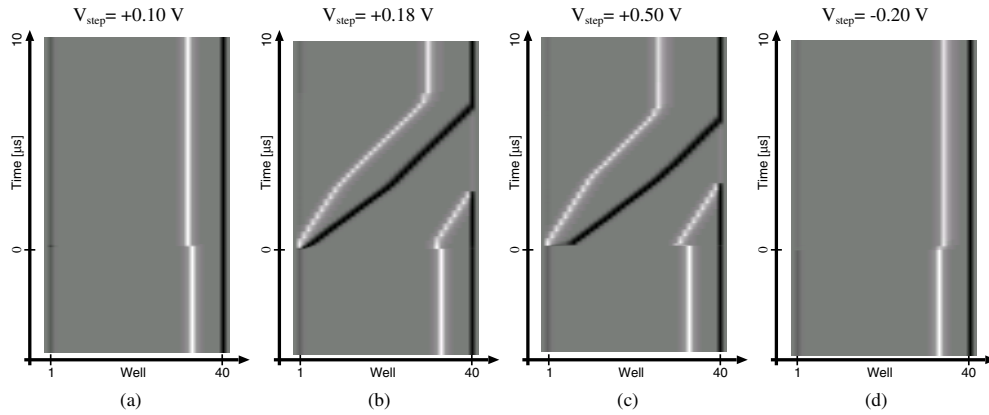
Figure 17. Evolution of electron densities in the quantum wells during the switching process for various voltage steps. White indicates high electron density (accumulation front), black indicates low electron density (depletion front). In the grey area the electron density is $\approx N_D$. Well No 1 is located at the emitter, well No $N = 40$ at the collector. At $t = 0$ a voltage step V_{step} is applied, starting from $V_i = 0.75$ (reprinted from [3]).

$I_u = eN_D^w v_M J_2/l$. For depletion waves, $n_i \ll N_D^w$ and $F_i - F_{i-1} \approx -eN_D^w/\varepsilon$, we can ignore the tunnelling current $J_{i \to i+1}$ in equation (3.3), and therefore the front velocity is approximately $J/(eN_D^w)$, i.e. a linear function of the current [11,36]. The point in figure 16 where the velocities of accumulation and depletion fronts intersect is of special interest: this point determines the velocity and current at which a dipole wave consisting of a leading depletion front and a trailing accumulation front can move rigidly [11].

Let us now consider a switching process where condition (5.2) is fulfilled and $V_{step} > 0$. The dynamical evolution of the electron densities n_i is depicted in figure 17(a) for $V_{step} = 0.1$ V. We observe that the charge monopole region of high electron density (light region) is shifted upstream (against the field eF) towards the emitter. This shifting occurs on a timescale of $0.1\ \mu$s, explaining the fast monotonic relaxation if equation (5.2) is fulfilled. The switching to a higher external voltage has the effect that all fields in the superlattice are increased and the current instantaneously rises above I_u. According to figure 16 this gives rise to a negative velocity of the accumulation front.

If condition (5.2) is violated, the switching scenario is more complicated. For $V_{\text{step}} = 0.18$ V and $V_{\text{step}} = 0.50$ V the evolution of the electron-density profile is depicted in figure 17(*b*) and (*c*), respectively. Before switching V_{step}, there is a charge accumulation front inside the sample corresponding to the domain wall separating two coexisting stationary high-field domains. After switching the voltage, the charge dynamics in the superlattice exhibits three different phases:

 (i) upstream shift of the accumulation front and generation of new fronts at the emitter;
 (ii) coexistence of three fronts in downstream motion; and
(iii) downstream motion of two fronts. These three phases will now be considered in detail.

Phase (i).   Shortly after switching the voltage step, the original pre-existing electron accumulation layer moves upstream towards the emitter. Simultaneously, a charge dipole wave appears at the emitter. Its leading depletion front moves towards the collector while its amplitude increases. The trailing electron accumulation front of the dipole is pinned at the first SL well.

The mechanism for the generation of a dipole at the emitter is as follows: in a stationary situation, the current through the emitter barrier is equal to the current through the first SL barrier. The field at the emitter can be calculated from equation (5.1). We assume a contact conductivity σ such that the dimensionless boundary current at the emitter, E/ρ (where $\rho = ev_M N_D^w/(\sigma F_M l)$ is the dimensionless contact resistivity), and the homogeneous, dimensionless current–field characteristic, $v(E)$, intersect on the second branch of the latter, at a critical value J_c. (We then have to choose the slope of the emitter current to be lower than the slope of the homogeneous low-field current–field characteristic.) If $0 < J < J_c$, the field at the emitter barrier is larger than that at the first barrier, $E_0 > E_1$. Then the Poisson equation predicts electron depletion, $n_1 < 1$. If we could suddenly change the current to a value larger than J_c, the field E_1 would increase according to equation (3.3), trying to attain a value on the third branch of the characteristic curve. This would produce an electron accumulation layer at this well followed by the depletion layer which was there before changing J. The net outcome of this mechanism would be the creation of a dipole. As seen in figure 16, a depletion layer separated from the contacts has to move towards the collector, at a speed $c_-(J)$ roughly proportional to J. As the depletion wavefront moves, it leaves a high-field region behind that extends all the way to the injecting region. The width of this region increases as its leading edge (the depletion wavefront) advances. The extra area gained by this region has to be compensated by lowering the current (for both the low-field and the high-field domain occur in a region of positive differential conductivity), so as to keep the total voltage constant. Once the current has become smaller than J_c, the field in the immediate neighbourhood of the injecting region should correspond to another depletion layer, which means that an accumulation wavefront forming the back of the pulse has been created meanwhile. Now the dipole is fully detached from the injecting region and a new phase starts.

Phase (ii).   After about $0.2\,\mu$s, the current has dropped below I_l, which, from figure 16, means that all fronts have positive velocities. In dimensionless units, for an instantaneous value of the current density J, accumulation fronts move with velocity $c_+(J)$ whereas depletion fronts move with velocity $c_-(J)$. Let us ignore the fast timescale responsible for the current spikes in figure 15(*a*) and try to find an equation for the envelope of the current–time trace. Then we can consider that the field profile adjusts adiabatically to the instantaneous value of the envelope of the current–time trace, $J(t)$, which evolves slowly. The electric field profile consists of an advancing dipole wave with field $E^{(3)}(J)$ (enclosed by an accumulation wavefront centred at

$i = m_+^{(1)}(t)$ and a depletion wavefront centred at $i = m_-^{(1)}(t)$), and an accumulation wavefront at $i = m_+^{(2)}(t)$ that encroaches on a high-field region with $E = E^{(3)}(J)$ near the collector contact. We can mark the centre of a wavefront at a time t as the well at which there is a local maximum (or minimum in the case of a depletion wavefront) of the charge. Then the functions $m_\pm^{(j)}(t)$ are integer valued, because the charge inside the wavefront peaks at different wells as time changes. Consider the lifetime of a given wavefront and denote by $t_1, t_2, \ldots$ the times at which $m_\pm^{(j)}(t)$ changes. We may define a local velocity by $c_\pm^i = [m_\pm^{(j)}(t_{i+1}) - m_\pm^{(j)}(t_i)]/(t_{i+1} - t_i)$. Let us assume that we average these $c_\pm^i$ over a time interval that is short compared to the timescale typical of wavefront motion, but sufficiently long compared to the mean value of $(t_{i+1} - t_i)$, for the wavefront to have advanced over many wells. Furthermore, as the envelope of the current–time trace varies slowly, the average of the $c_\pm^i$ can be approximated by $c_\pm(J)$, where J is the instantaneous value of the envelope of the current–time trace. The average wavefront velocities are

$$\left\langle \frac{\mathrm{d}m_+^{(j)}}{\mathrm{d}t} \right\rangle = c_+(J), \qquad \left\langle \frac{\mathrm{d}m_-^{(j)}}{\mathrm{d}t} \right\rangle = c_-(J), \qquad j = 1, 2. \tag{5.3}$$

We can now calculate easily the dimensionless voltage ϕ corresponding to the field profile considered above (one advancing pulse and one accumulation wavefront at the end of the SL). Ignoring transition regions, we obtain

$$\phi = \frac{1}{N} \sum_{j=1}^{N} E_i = E^{(1)}(J) + [E^{(3)}(J) - E^{(1)}(J)] \left(\frac{N - m_+^{(2)}}{N} + \frac{m_-^{(1)} - m_+^{(1)}}{N} \right). \tag{5.4}$$

We now differentiate this equation with respect to t, use $\mathrm{d}\phi/\mathrm{d}t = 0$, average over short time intervals as indicated above, and use equation (5.3). Then we obtain the following equation for J (the envelope of the current–time trace):

$$\frac{\mathrm{d}J}{\mathrm{d}t} = \frac{2c_+(J) - c_-(J)}{N} \frac{[E^{(3)}(J) - E^{(1)}(J)]^2}{\frac{E^{(3)}(J) - \phi}{v'(E^{(1)}(J))} + \frac{\phi - E^{(1)}(J)}{v'(E^{(3)}(J))}}. \tag{5.5}$$

Notice that if we had started from a field profile comprising n_+ moving accumulation wavefronts and n_- depletion wavefronts, the same arguments would lead to the more general equation

$$\frac{\mathrm{d}J}{\mathrm{d}t} = \frac{n_+ c_+(J) - n_- c_-(J)}{N} \frac{[E^{(3)}(J) - E^{(1)}(J)]^2}{\frac{E^{(3)}(J) - \phi}{v'(E^{(1)}(J))} + \frac{\phi - E^{(1)}(J)}{v'(E^{(3)}(J))}}. \tag{5.6}$$

J evolves on the timescale t/N, which is slow provided N is large. Clearly, J given by equation (5.5) changes until it reaches a value $J^\dagger$ such that $2c_+(J) = c_-(J)$. This means that the original accumulation layer and the trailing accumulation front start advancing towards the collector with the same velocity $c_+(J^\dagger)$, while the positively charged leading front of the dipole moves towards the collector at a higher velocity $c_-(J^\dagger)$. Numerical simulations of different discrete models [3, 67, 68] show that each time an accumulation layer advances by a SL period, a spike of the current appears. An asymptotic theory explaining this fact is still lacking. If we accept it at face value, the double-peak structure observed in the numerical simulation of figure 15(a) means that two accumulation wavefronts exist during that part of the period. Notice that the transient region where the current exhibits double spikes has a flat appearance, indicating the constant *mean value* of the current, $J^\dagger$. This is further corroborated by figures 17(b) and (c). In these figures, time traces of the positions of all wavefronts are recorded. Velocities are the reciprocals of the slopes. Notice that the velocity of the depletion wavefront constituting the leading edge of the dipole wave, $c_(J)$, is larger than the velocity of the two accumulation wavefronts that coexist during a short time interval after $t = 0$. When the

accumulation wavefront closer to the receiving region exits, phase (ii) ends and a new phase, phase (iii), starts. As observed in figures 17(b) and (c) and explained below, the slopes of the accumulation and depletion wavefronts enclosing the high-field region become identical and their corresponding velocity is smaller than $c_-(J^\dagger)$ during phase (ii).

Please note that the above explanation is heuristic and that a consistent asymptotic argument should replace it in the future. Such an argument should explain the spikes in the current–time trace and still retain equation (5.6) (conveniently reinterpreted as necessary).

Phase (iii). After the original accumulation layer has reached the collector at $t_0 \approx 3 \mu$s, there are only one accumulation layer and one depletion layer present in the sample, giving rise to a single-spike structure of the current response as depicted in figure 15(a). The same reasoning as in relation to phase (ii) leads us to equation (5.6) with $n_+ = n_- = 1$. After a short transient, the velocities of the positively and negatively charged fronts should become equal, $c_+(J) = c_-(J)$. This occurs at a current $J = J^*$ corresponding to the crossing point of the two front velocities, as depicted in figure 16. In comparison to that for phase (ii), the velocity of the accumulation front has almost doubled, while the velocity of the depletion front has decreased slightly. See figures 17(b) and (c).

After these three stages of its evolution, the accumulation front finally reaches a stable stationary state: it becomes the domain wall separating two stationary high-field domains. Of all such possible stationary solutions at voltage $V_{dc} + V_{step}$, the one having an accumulation layer closer to the emitter is reached. This final situation on a low-current branch of the I–V characteristic at voltage $V_f = V_{dc} + V_{step}$ could also be reached by conventional down-sweeping of the I–V characteristics. In the latter case, the electron accumulation layer also moves towards the collector.

For $V_{step} < 0$, the electron accumulation layer always travels towards the collector and stops at a position corresponding to the domain wall separating low- and high-field domains of a stationary solution. This solution is the same as that which could be reached by down-sweeping to the final voltage; see figure 17(d). In contrast to the case for positive V_{step}, the resulting current response shows no threshold-like behaviour; see figure 15(b). Since all fields decrease during the switching process, no dipole wave can be generated at the emitter.

6. Self-sustained oscillations of the current

Self-sustained oscillations of the current in weakly coupled SL were experimentally observed a few years ago and interpreted on the basis of the discrete drift model [52]. Self-oscillations are caused by recycling and motion of waves in a dc voltage-biased SL. Depending on contact conditions, these waves may be charge accumulation layers (monopoles or wavefronts) or electric field pulses (charge dipoles) [67]. Both types of wave are found in the DDD model assuming that the injecting contact is described by Ohm's law with appropriate resistivity [3], a result common to the Gunn effect in bulk GaAs [36]. The asymptotic theory for the Gunn effect can be used to describe analytically self-oscillations in the continuum limit [10, 11, 36]. This description leaves out effects due to the discrete nature of the equations, such as current spikes [67]. In this section, we shall describe the asymptotic theory of self-oscillations, and the effect of parameters such as doping, temperature, and photoionization on oscillation frequency and amplitude.

6.1. Asymptotic theory

In the continuum limit $v \to 0$, $L \equiv Nv \gg 1$, the equations for electric field and current density are equation (4.14) and the voltage bias condition (3.13), which becomes

$$\frac{1}{L} \int_0^L E(x, t)\, \mathrm{d}x = \phi. \tag{6.1}$$

Appropriate boundary conditions can be equations (5.1), together with Ampère's law (3.7) at $i = 0$ and at N. We can write these equations in dimensionless units by using table 1 at the end of section 3, noticing that the dimensionless tunnelling currents are $(J - \partial E/\partial t)$. The results are

$$E(0, t) = \rho\left(J - \frac{\partial E(0, t)}{\partial t}\right),$$
$$n(L, t)E(L, t) = \rho\left(J - \frac{\partial E(L, t)}{\partial t}\right), \tag{6.2}$$

where $\rho = eN_D^w v_M/(\sigma F_M l)$ is the dimensionless contact resistivity. Equation (4.14) is the hyperbolic limit of the Kroemer model for the Gunn effect in bulk n-GaAs (with zero diffusivity). Knight and Peterson [43] had already shown in 1966 that, at constant J, this equation may develop shock waves (our approximations to the wavefronts). The difference from the model for the Gunn effect is that the shock velocities are given by (4.15), (4.18), and (4.19) in section 4 instead of the usual equal-area rule for the Gunn effect [43]. Except for this difference and the peculiarities introduced by our boundary conditions, we can use the asymptotic theory of the Gunn effect to understand current self-oscillations in a SL. In an incomplete form, this theory was introduced in [36] (for ohmic boundary conditions) and later elaborated (for different boundary conditions) in [11].

The key to understanding self-oscillations is to realize that the (monopole or dipole) waves are small compared to the dimensionless SL length ($L = Nv = NeN_D^w/(\varepsilon F_M) \gg 1$) in the limit we consider. Outside the wavefronts, we can therefore rescale time and length as $s = t/L$ and $y = x/L$, so (4.14) and (6.1) become

$$J - v(E) = \frac{1}{L}\left[\frac{\partial E}{\partial s} + v(E)\frac{\partial E}{\partial y}\right], \tag{6.3}$$

$$\int_0^1 E(y, s)\, \mathrm{d}y = \phi, \tag{6.4}$$

where $1/L \ll 1$ is a small parameter. Notice that, according to table 1 in section 3, the unit of time is $l/(v_M v)$. Then the dimensionless time t is $v v_M t_d/l$ where t_d is time measured in seconds (for instance). The 'slow' dimensionless time s is obtained by dividing t by $L = Nv$, so it is $s = v_M t_d/(Nl)$. Nl/v_M is the order of magnitude of the time that an electron would need to traverse the SL, while $l/(v_M v)$ gives the order of magnitude of the time that an electron would take to traverse one SL period. The ratio of these two times is $L = Nv \gg 1$. Similarly, the 'slow' spatial variable $y = x/L = i/N$, where i is the index of the SL period that we are considering (i.e., the discrete variable in section 3).

As $L \gg 1$, equation (6.4) yields $v(E) = J$ outside the wavefronts, i.e., the field is either $E^{(1)}(J)$ or $E^{(3)}(J)$ there. The current density J evolves in the slow timescale, $J = J(s)$, so we may consider J as a constant when constructing the wavefronts. These will then be described as explained in section 4. We shall now describe asymptotically one time period of the current self-oscillation starting from a given field configuration inside the SL. The initial profile will evolve with time following the current adiabatically and our first goal will be to find an evolution equation for J. The easiest imaginable dynamic situation for an initial field profile is that we have only one monopole or one dipole inside the SL.

Monopole.   If a monopole joining $E^{(1)}(J)$ to $E^{(3)}(J)$ is at $x = X^+(t)$ (equivalently, at $y = X^+/L = Y^+$), the bias (6.1) is given by

$$\phi \sim E^{(1)}(J)Y^+ + E^{(3)}(J)(1 - Y^+). \tag{6.5}$$

If we differentiate this equation with respect to time and use $dX^+/dt = dY^+/ds = C(J)$ together with (6.5), we obtain

$$\frac{dJ}{ds} = \frac{[E^{(3)}(J) - E^{(1)}(J)]^2}{\frac{E^{(3)}(J) - \phi}{v'(E^{(1)}(J))} + \frac{\phi - E^{(1)}(J)}{v'(E^{(3)}(J))}} C(J). \tag{6.6}$$

Since $C(J) > 0$, the current increases as the monopole moves. Notice that equation (6.6) is a particular case of equation (5.6) with $n_+ = 1$, $n_- = 0$, $c_+ = C(J)/v$, and $s = t/L$.

Dipole.   A dipole consists of a region where the field is $E^{(3)}(J)$, moving towards the anode. Its trailing edge is a monopole at $x = X^+(t)$ (equivalently, at $y = X^+/L = Y^+$), joining $E^{(1)}(J)$ to $E^{(3)}(J)$. The dipole leading front is a region depleted of electrons: $E = -x + \int J \, dt$, and located at $y = Y^-$. Its velocity is clearly $dY^-/ds = J$. The bias (6.1) is now

$$\phi \sim E^{(1)}(J) + [E^{(3)}(J) - E^{(1)}(J)](Y^- - Y^+). \tag{6.7}$$

If we differentiate this equation with respect to time and use $dY^+/ds = C(J)$ and $dY^-/ds = J$ together with (6.5), we obtain

$$\frac{dJ}{ds} = \frac{[E^{(3)}(J) - E^{(1)}(J)]^2}{\frac{E^{(3)}(J) - \phi}{v'(E^{(1)}(J))} + \frac{\phi - E^{(1)}(J)}{v'(E^{(3)}(J))}} [C(J) - J], \tag{6.8}$$

which is a particular case of equation (5.6) with $n_+ = n_- = 1$, $c_+ = C(J)/v$, $c_- = J/v$, and $s = t/L$. Now the current evolves towards $J = J^*$ such that $C(J^*) = J^*$. We observe that the dipole moves at constant current with velocity given by the equal-area rule (4.16), $V(E^{(1)}, E^{(3)}) = J$. After $Y^- = 1$, there is only one monopole in the SL and we are back at equation (6.6). Again, the current increases as the monopole moves.

Instability at the injecting contact.   Near the injecting contact at $y = 0$, we have a boundary layer where the field profile adiabatically follows $J(s)$ according to

$$\frac{\partial E}{\partial x} \sim \frac{J}{v(E)} - 1, \qquad E(0, s) = \rho J. \tag{6.9}$$

Notice that we have ignored $\partial E/\partial t = L^{-1} \partial E/\partial s \ll 1$. Typically, the contact resistivity is chosen such that: either (i) $0 < \rho < 1$ and the straight line $j = E/\rho$ does not intersect the curve $j = v(E)$; or (ii) $\rho > 1$ and $j = E/\rho$ intersects $j = v(E)$ at (E_c, J_c) with $1 < E_c < E_m$ (on the second branch of $v(E)$).

As x departs from the cathode, $E(x, s)$ has to reach the constant solution of $J - v(E) = 0$ which is found to the left of the accumulation layer moving towards the anode (either a monopole or the back of a dipole, depending on the value of the contact resistivity). If $v_m < J < J_c$, the appropriate field value to the left of the accumulation layer is $E^{(1)}(J)$. Thus $E(x, s)$ either increases monotonically from ρJ to $E^{(1)}(J)$ in case (i), or it decreases monotonically from ρJ to $E^{(1)}(J)$ in case (ii). Assume that we just have one monopole left in the SL (in case (ii) this means that the leading front of the dipole has already reached the SL end). Then $J(s)$ increases according to (6.7) until it surpasses $J = 1$ in case (i) or $J = J_c$ in case (ii). In the first case, $E(x, s)$ keeps the same shape, only now the field at the left of the monopole and outside the cathode layer would try to leave $E = 1$ and tend towards $E^{(3)}(J)$, $J \approx 1$. This situation is unstable, a new monopole is created at the cathode, and J decreases
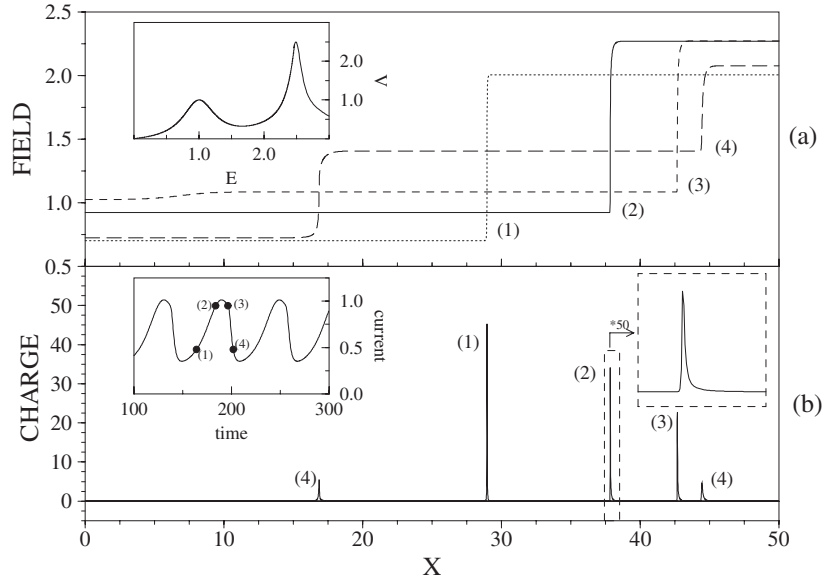
Figure 18. (*a*) Time evolution of the electric field profile on the SL obtained using the velocity curve shown in the inset. (*b*) Charge-density profiles, $n - 1 = \partial E(x, t)/\partial x$, showing the location of the wavefront for different times. The total current density versus time is shown in the leftmost inset, in which we have marked the times corresponding to the profiles depicted in part (*a*). The rightmost inset shows clearly a monopole with a right tail (reprinted from [10]).

below 1 [10, 36]. For a very short time, the newly created monopole joins $E^{(1)}(J)$ to $E^{(2)}(J)$, while the old one joins $E^{(2)}(J)$ to $E^{(3)}(J)$. Then the old monopole disappears rapidly. It is important to notice that the charge inside the new monopole is not appreciable until it has departed sufficiently far from the cathode region. See figure 18 and details of asymptotic calculations in [10]. Notice that, in the last reference, the boundary condition at the cathode $x = 0$ is $\partial E/\partial x = c$ and that part of the calculation has to be slightly modified if the boundary condition (6.2) is used instead.

In case (ii), $E^{(1)}(J)$ still exists at $J = J_c < 1$. As J surpasses J_c, the solution for the contact equation (6.9) would tend to increase towards $E^{(3)}(J)$ as x increases, but far from the cathode the field is still $E^{(1)}(J)$. As explained in the previous section, this is an unstable situation that gives rise to dipole creation at the cathode [11, 36]. The details of the fast wave nucleation at the cathode can be found in [11] (again a slight modification in the calculations is needed if we use the boundary condition (6.2) instead of the one used in the cited reference). After a new wave is created, J decreases. Then inside the SL there are either two monopoles in case (i) or one monopole and a dipole in case (ii). In the latter case and provided that ϕ is sufficiently large, we obtain equation (5.5) with $s = t/L$, $c_+ = C(J)/v$, and $c_- = J/v$. Then J tends to $J = J^\dagger$ such that $2C(J) = J$. Provided $J^\dagger < J_c$, J stays at the value $J^\dagger$ until the old monopole exits from the sample and we are back at the initial situation. The description of one period of the self-oscillation in case (i) is somewhat more complicated during the stage where two monopoles coexist [10]. In any case one of the monopoles is eventually destroyed and we have completed one period of the oscillation. If $J > J^\dagger$ in case (ii), it is theoretically possible to create several dipoles and to produce a chaotic current signal [19]. This seems to have been observed numerically by Amann *et al* [4], who used the discrete model with a general constitutive relation for the tunnelling current as in appendix A. Whether this possibility can be realized in an experimental situation remains to be seen.

It is important to highlight the far-reaching difference between the monopole- and dipole-mediated self-oscillations that we have mentioned before: dipoles are created fast and therefore contain noticeable charge accumulation and depletion layers that travel through (almost) the whole SL. On the other hand, monopoles are also created at the injecting contact, but the charge accumulation in them becomes noticeable only after a certain build-up time. This means that monopoles apparently traverse part of the SL during an oscillation period whereas dipoles traverse the whole SL. Obviously this difference has important consequences that may be experimentally testable: monopole-mediated oscillations have higher frequencies. Furthermore, numerical simulations of discrete models show that each time a charge accumulation layer jumps from well to well, a current spike is produced. Then the number of current spikes per oscillation period (seen in simulations of discrete models, not in the continuum limit) is smaller for monopole self-oscillations than in the case of dipole-mediated oscillations; see the numerical results in [67] and section 2.

6.2. Dependence of the oscillations on control parameters

It is important to learn how the frequency and amplitude of current self-oscillations depend on the configuration of the SL (doping, barrier and well widths, number of SL periods) and other parameters, such as voltage, temperature, magnetic field, photoexcitation, that can be controlled. We have explained previously how the boundary condition at the cathode selects whether monopole or dipole recycling and motion characterize the self-oscillation. In essence a cathode condition that imposes a charge accumulation layer near the cathode for all values of the current selects monopole recycling. Besides Ohm's law with low resistivity, an excess of electrons in the first SL period,

$$n_1 - 1 = c > 0 \Longrightarrow E_0 = E_1 - cv \qquad (6.10)$$

has also been widely used to select monopoles [9, 10, 15, 40].

6.2.1. Doping.
Figure 19 shows a doping–voltage phase diagram for the second plateau (thereby zero diffusivity) of a 20-well SL, assuming that the cathode condition is (6.10) with $c = 10^{-4}$ [55]. For dimensionless doping lower than the minimum of the solid line, the SL evolves towards an almost uniform stationary state. For larger doping with $v < v_{TB}$, we have a almost uniform, stable stationary state outside a certain bias interval $(\phi_\alpha, \phi_\omega)$. At these points, a branch of self-oscillations bifurcates stably (supercritically) starting with zero amplitude and nonzero frequency (Hopf bifurcation). For $v > v_{TB}$, a horizontal line intersects a number of different curves: (i) Hopf bifurcations, (ii) saddle-node bifurcations, (iii) homoclines. Intersecting several Hopf bifurcation curves may indicate that there are intervals of self-oscillations alternating with intervals where the stable solution is a stationary state. The stationary state is a pinned wavefront (or monopole) separating two electric field domains at which E_i is either $E^{(1)}(J)$ or $E^{(3)}(J)$. The wavefront is pinned at a well M such that $\phi \approx E^{(1)}(J)(M/N) + E^{(3)}(J)(1 - M/N)$. There may be at most N intervals of stationary wavefronts. Between two such intervals, there may be a bias interval of stable self-oscillations in which monopole recycling and motion occurs about the Mth well. In some of the interior regions observed for such doping values, there may be coexisting multistable states with hysteresis cycles in their transitions from one to the next. The last interval of self-oscillations ends at a homocline—that is, the oscillation frequency tends to zero while the amplitude remains finite. Another interesting feature of the phase diagram is the dashed line of Hopf bifurcations above the point marked DH. On this line, the Hopf bifurcation is subcritical—that is, an unstable branch of self-oscillations bifurcates for $\phi < \phi_\alpha$. Typically
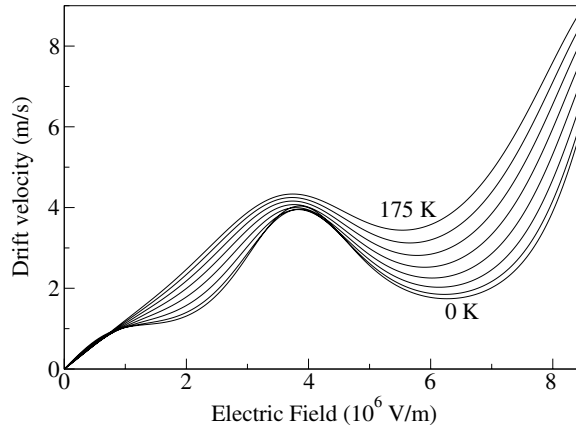
Figure 19. The total phase diagram of the model for $N = 20$ and $c = 10^{-4}$. The dotted curves are curves of stationary saddle nodes. For the sake of clarity, we have plotted only the main line of homoclinic orbits which sprout from the Takens–Bogdanov point TB (thin solid curve; at a Takens–Bogdanov point, lines of Hopf bifurcations, saddle-node bifurcations, and homoclinic orbits intersect tangentially). We have not shown other homoclinic orbits: there is one curve of homoclinic orbits for each Hopf curve (reprinted from [55]).

(This figure is in colour only in the electronic version)

this branch coalesces with a branch of stable oscillations at a smaller bias ϕ_{LP}. Then there is an interval where both self-oscillations of finite amplitude and frequency and a stationary state are stable (interval of bistability). Driving the bias adiabatically, we can obtain a hysteresis cycle. Finally, for large enough doping, the self-oscillations disappear and we have multistability of stationary solutions corresponding to coexistence of domains separated by a pinned wavefront.

The previous phase diagram may change substantially if we change the number of SL periods or c. For example, the branch of self-oscillations may disappear in the high-bias region either at a Hopf bifurcation (finite frequency) or at a homoclinic orbit (zero frequency), depending on the values of these parameters. The frequency may decrease or increase with increasing bias. The first situation was observed in [40], and the second in [85].

6.2.2. Temperature. Temperature changes both the Fermi functions and the scattering amplitudes in the expressions for the tunnelling currents. As a consequence, drift velocity and diffusion coefficients in the DDD model can be substantially changed, which in turn can drastically affect self-oscillations.

Figure 20 depicts the field-dependent drift velocity at different temperatures for SL parameter values of [84]: 40 periods of 14 nm GaAs and 4 nm AlAs and well doping $N_D^w = 2 \times 10^{11}$ cm^{-2}. It has been calculated from the microscopic tunnelling current density by the procedure explained in [12]. The only adjustable parameter in the sequential tunnelling formulae is the Lorentzian half-width of the scattering amplitudes, γ. To estimate them, we have assumed that the voltage difference, ΔV, between the peaks of two consecutive branches on the second plateau of the static I–V characteristic is

$$\Delta V \approx \mathcal{E}_{C3} - \mathcal{E}_{C2} - 2\eta\gamma. \tag{6.11}$$

Figure 20. Drift velocity versus electric field for different temperatures (starting at 0 K up to 175 K in 25 K steps) for a 40-well 14 nm GaAs/4 nm AlAs SL. The well doping is $N_D^w = 2 \times 10^{11}$ cm^{-2} (reprinted from [69]).

Here $\mathcal{E}_{Ci}$ is the ith energy level of a given well. For $\gamma = 0$, the field profile on the second plateau corresponds to two coexisting electric field domains with fields $(\mathcal{E}_{C2} - \mathcal{E}_{C1})/(el)$ and $(\mathcal{E}_{C3} - \mathcal{E}_{C1})/(el)$. The domain walls corresponding to two adjacent branches in the I–V diagram are located in adjacent wells. Then the voltage difference should be $\Delta V \approx (\mathcal{E}_{C3} - \mathcal{E}_{C2})/e$. In the presence of scattering, resonant peaks have finite widths which we take as $2\eta\gamma$, thereby obtaining (6.11). 2η is an adjustable parameter of the order of unity [29]. By using this formula and the measured current in [84] (figures 1–3), we find $\gamma = 18$ meV at 1.6 K and $\gamma = 23$ meV at 140 K for $\eta \approx 0.6$. Linear interpolation yields the temperature dependence of γ in the range that we are interested in.

Notice that the first peak of the velocity in figure 20 (see the shoulder feature at about 106 V m^{-1} for temperatures below 50 K) rapidly disappears as the temperature increases for this particular sample. This result might change if we assume different scattering amplitudes for each of the first two subbands of the wells. Moreover, the different extrema of the velocity curve shift to lower field values as the temperature increases. Thus formation of electric field domains and current self-oscillations are expected for voltages on the second plateau and higher. Multistable solution branches of the I–V characteristic curve should also shift to lower voltages and higher currents as the temperature increases, as observed in experiments [46]. These effects could not be obtained from the fitted drift velocity in [46]. As the diffusion coefficient decreases very rapidly with field, we can safely set $D \equiv 0$ in our DDD model for the experimentally observed voltage range. The relevant model is thus the well-known discrete drift model of [9] with the drift velocity of figure 20 and the boundary condition (6.10). Results of numerical calculations are shown in figure 21. We observe that the I–V curve presents intervals in which the average current increases with voltage, followed by intervals in which the average current decreases. At lower temperatures the intervals of increasing current are wider whereas the opposite occurs at higher temperatures. Correspondingly, the frequency of the self-oscillations in such an interval starts increasing but it drops to a smaller value than the initial one at the upper limit of the interval. The amplitude of the self-oscillations (not shown here) vanishes at the upper and lower limits of each voltage interval. This suggests that the branches of self-oscillations begin and end at supercritical Hopf bifurcations. As the temperature increases, the region of negative differential conductivity in figure 20 becomes smoother and the frequency of
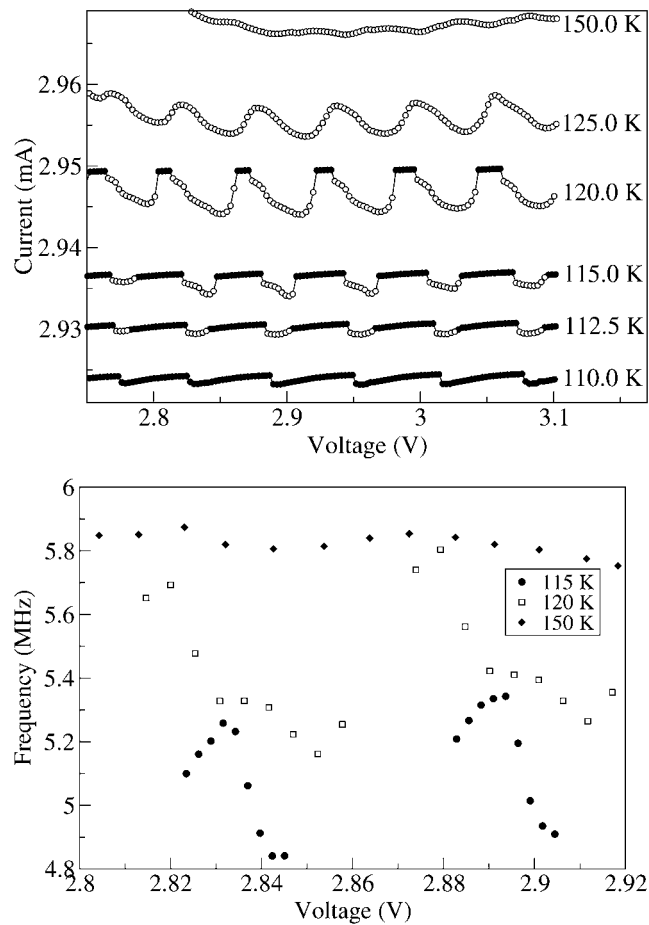
Figure 21. (*a*) *I–V* characteristics for different temperatures, showing stationary (dynamic) states with full (empty) circles. The boundary condition parameter $c = 10^{-3}$ has been used in the numerical simulations. The curve corresponding to 150 K has been shifted by -0.04 mA for clarity. Lines are plotted only for eye-guiding purposes. (*b*) Current oscillation frequency versus voltage for some dynamic dc bands of the curves shown in (*a*) (reprinted from [69]).

the self-oscillations increases; see figure 21(*b*). At low temperatures, the electric field profiles consist of basically two stationary domains joined by a domain wall. The *I–V* characteristic curve has multiple branches corresponding to stationary domains with the domain wall located at different wells. This situation resembles that obtained as voltage and doping are varied, provided doping and inverse temperature are assimilated. Notice in figure 21 that there are voltage intervals where the oscillation frequency increases with voltage, while the average current decreases with voltage. This behaviour was called *anomalous* by Wang *et al* [85] but it can be directly explained by the discrete drift model equations; see [69].

6.2.3. Effect of other parameters on self-oscillations. The effect of other parameters such as photoexcitation or an external magnetic field on electric field domains [50] or self-oscillations [51, 78, 79] has been explored both experimentally and theoretically, although not to the same extent as in the cases of doping and temperature.

The influence on self-oscillations of a magnetic field B transverse to the SL growth direction has been studied experimentally and theoretically by Sun *et al* [78, 79]. They found that increasing the magnetic field was qualitatively similar to increasing the temperature in a doped SL that presented a multistable field domain configuration. Their SL presented such a configuration at $B = 0$ T. Increasing B both shifted the plateaus to larger voltages and diminished the length of the branches in the $I–V$ characteristic curve and the peak current. Above a critical field, the $I–V$ curve became flat and self-oscillations started. If a higher critical B was surpassed, the self-oscillations disappeared and so did the corresponding plateau. These observations were explained by simulations of the discrete drift model with parameters corresponding to the second plateau of the SL [79]. For the drift velocity, Sun *et al* used the Kazarinov–Suris expression [41] in which the Lorentzian width increased with B and its centre, eFl, changed to $eFl - e^2l^2B^2/(2m^*)$. It would be interesting to compare experimental results with those for similar simulations using the drift velocity (A.12).

Photoexcitation acts on self-oscillations qualitatively similarly to doping [8, 52, 58, 59]. Discrete models are somewhat more complicated. We have to consider the two-dimensional hole density in the Poisson equation and add a rate equation for it [8, 34]. Phase diagrams of photoexcitation versus voltage and frequency dependence of the self-oscillations have been studied experimentally [59], but more theoretical work is needed to explain them [62].

7. Final remarks

We have reviewed nonlinear charge transport in weakly coupled semiconductor SL. Key experimental results indicate that the governing equations are spatially discrete, and demonstrate that the formation and dynamics of electric field domains are responsible for many interesting phenomena such as multistability and hysteresis between stationary configurations and self-oscillations of the current. In this article, we have discussed the basic theory of stationary states and wavefronts in simple discrete DDDs for charge transport in a SL. The core of this theory is consideration of wavefronts in an infinitely long SL under constant current bias. Depending on doping and the value of the current, wavefronts joining two stable constant field values may be stationary or move upstream or downstream with the flow of electrons. It turns out that the smooth profile of a moving wavefront becomes discontinuous and gives rise to a stationary wavefront as the current approaches certain (doping-dependent) critical values. Explicit formulae for the wavefront velocity can be obtained in two limits: the strongly discrete (large doping) and the continuum limit (small doping).

Finite SL under voltage bias may exhibit the above-mentioned multistability of stationary field configurations or self-sustained current oscillations. The results for infinitely long SL can be used to understand these different situations provided the SL is long enough. So far, asymptotic calculations have been performed in the continuum limit and used to understand numerical solutions of the discrete models. Depending on the boundary condition at the injecting contact, self-oscillations may be due to the recycling and motion of either charge monopole or dipole waves [12, 36, 67, 83]. The influence of control parameters such as doping, temperature, external magnetic fields, and laser photoexcitation can be theoretically studied by means of discrete models, although relatively complete work has been carried out only in the case of doping [55]. Let us comment now on different research avenues in which further work seems worthwhile:

 (1) relocation of electric field domains and charge fluctuations;
 (2) SL with disorder;
 (3) discrete hydrodynamics;
 (4) aperiodic dynamics.

(1) Relocation of domains and charge fluctuations. In relocation experiments, a doped SL displaying a multistable $I-V$ characteristic is biased (typically) on the first plateau, say in the middle of a branch. The corresponding field configuration has two domains separated by a domain wall which is an accumulation layer. Then the voltage is suddenly increased from V_0 to $V_1 = V_0 + \Delta V$ and the time evolution of the current is recorded. Depending on ΔV, the domain wall has to relocate in such a way that a stable field configuration appropriate to the new voltage is reached [49]. The outcome has been studied numerically using the discrete model given by equations (3.1) and (3.3) with a constitutive relation of the form (A.8) and ohmic boundary conditions (5.1) [3]. For any $\Delta V < 0$ as well as for small positive ΔV, the relocation of the domain wall always occurs by a direct movement of the charge monopole forming the domain boundary to its final position. This movement may be either upstream or downstream in the electron flow as needed. However, for sufficiently large $\Delta V > 0$, a charge dipole is injected at the emitter contact in addition to the existing monopole, because the latter cannot move upstream beyond one SL period without encountering a stable field configuration [3]. Recent experiments by Rogozia *et al* [65] confirm this theoretical picture. It seems desirable to extend the theory of active wells (strongly discrete limit) to give a better asymptotic explanation of the numerical solution than that in section 5. Other experiments have shown that the relocation time for up jumps ($\Delta V > 0$) close to the discontinuity in the $I-V$ characteristic is random and have also investigated its probability distribution function [64]. The corresponding theory will have to include shot noise terms in the governing equations and has not been analysed as yet although there are promising results of numerical simulations [13].

(2) SL with disorder. The effect of a random distribution of doping in the SL wells has been studied by means of numerical solutions of discrete models under voltage bias by Schöll's group [71,72] and compared with experimental results [80]. Their results explain the irregular appearance of static multistable branches in the experimentally observed $I-V$ characteristic of figure 1(*a*) [80]. The effect of disorder on wavefront motion and self-oscillations is less understood [61,71,72]. Interesting results could be obtained by means of the theory of active wells of [27]. It can be argued that the average wavefront speed scales with current as $|J - J_c|^{3/2}$ in the presence of disorder [28]. This contrasts with the classical critical exponent 1/2 of equation (4.13). The catch is that this novel exponent could be observed in experiments under dc current bias, not under the more usual dc voltage bias.

(3) Discrete hydrodynamics. Recently it has been argued that experimentally observed self-oscillations in certain strongly coupled SL can be explained by using a discrete model having different electron temperatures in different SL periods [77]. It would be interesting to derive discrete hydrodynamic equations for electron density, momentum, and temperature plus electric potential from a quantum kinetic formulation. Despite many advances reported in the quantum kinetic literature for SL [83], to this day neither discrete hydrodynamics or simpler discrete drift-diffusion equations have been derived from quantum kinetic equations. These derivations constitute an important open problem.

(4) Periodic and aperiodic dynamics. As indicated in section 6, a number of issues concerning self-oscillations under dc voltage bias are still not resolved despite their interest for comparison between theory and experiments. Phase diagrams (cf figure 19) including the dependence on the number of SL periods and boundary parameters are totally lacking; this may be due to the computational cost of running numerical continuation algorithms, although there is some work in progress on phase diagrams including temperature and photoexcitation.

Under ac + dc voltage bias, driven SL may exhibit aperiodic oscillations, either quasiperiodic or chaotic. This was predicted on the basis of numerical solution of the discrete drift model in [15, 16]. Experimental evidence was reported in [17, 48, 51, 87]. Numerical solution of a more detailed sequential tunnelling discrete model [1] shows that certain features of aperiodic behaviour may be due to the high-frequency current spikes superimposed on a natural self-oscillation as in figure 4; see [68]. In turn, this points to nontrivial effects caused by well-to-well wavefront motion during self-oscillations. To achieve a more analytical understanding of these effects, one should use the theory of active wells to describe wavefront motion in these more complex circumstances. If satisfactorily developed, this theory might also clarify the origin and mechanism of the chaotic oscillations under dc voltage bias numerically found by Amann *et al* [4]. Apparently these chaotic oscillations are due to random firing of wavefronts at the injecting contact due to a delicate choice of the contact resistivity, as explained for a bulk semiconductor in [19]. These chaotic oscillations have been predicted to occur for a SL dc voltage biased on the first plateau of the $I-V$ characteristic curve. However, in experiments, chaotic oscillations under dc voltage bias have only been observed in a SL biased on the second plateau [87, 88].

Chaotic oscillations are also possible in strongly coupled SL under ac + dc voltage bias [20, 21] or in regimes of negative effective mass induced by terahertz radiation [22, 23]. These predictions are based on numerical solution of continuum balance equation models. Predictions of chaotic dynamics for mathematically similar models of nonlinear transport in bulk n-GaAs under ac + dc voltage bias were made earlier [54, 60].

Acknowledgments

Appendix A. Tunnelling current and approximations

In this appendix, we derive simplified constitutive relations for the tunnelling current density across barriers in terms of the local electric field and the electron densities at adjacent wells. They clarify the range of validity of the DDD and discrete drift models. These derivations give leading-order asymptotic results that should be corrected if quantitatively precise formulae are needed. The formulae that we obtain have the advantage over pure numerical computations of being analytical and they can be used to develop the theory further. Given a known configuration of a sample used in experiments, our formulae allow calculation of constitutive relations that can be easily used to determine the dynamical behaviour of the SL.

We shall start by writing out the tunnelling current across the ith barrier given by the THM [12]:

$$J_{i \to i+1} = \frac{\hbar k_B T}{2m^*} \sum_{j=1}^{n} \int_0^{\infty} A_{C1}(\epsilon) A_{Cj}(\epsilon + eF_i l) \mathcal{T}_i(\epsilon) \ln \left[\frac{1 + \exp(\frac{\mu_i - \epsilon}{k_B T})}{1 + \exp(\frac{\mu_{i+1} - eF_i l - \epsilon}{k_B T})} \right] d\epsilon. \qquad (A.1)$$

Green function calculations yield the same expression except that $\mathcal{T}_i(\epsilon)$ is given by a different formula [3]. Here $A_{Cj}(\epsilon)$ is a Lorentzian function, $(\gamma_{Cj}/\pi)[(\epsilon - \mathcal{E}_{Cj})^2 + \gamma_{Cj}^2]^{-1}$, centred at the

energy of the jth subband and whose width is proportional to the reciprocal of the scattering time. $\mathcal{T}_i(\epsilon)$ is proportional to the transmission dimensionless transmission probability across the ith barrier:

$$\mathcal{T}_i(\epsilon) = \frac{16k_i^2 k_{i+1}^2 \alpha_i^2 (k_i^2 + \alpha_i^2)^{-1}(k_{i+1}^2 + \alpha_i^2)^{-1}}{(w + \alpha_{i-1}^{-1} + \alpha_i^{-1})(w + \alpha_{i+1}^{-1} + \alpha_i^{-1})e^{2\alpha_i d}},$$

$$\hbar k_i = \sqrt{2m^*\epsilon}, \qquad \hbar k_{i+1} = \sqrt{2m^*[\epsilon + e(d+w)F_i]},$$

$$\hbar\alpha_{i-1} = \sqrt{2m^*\left[eV_b + e\left(d + \frac{w}{2}\right)F_i - \epsilon\right]},$$

$$\hbar\alpha_i = \sqrt{2m^*\left(eV_b - \frac{ewF_i}{2} - \epsilon\right)},$$

$$\hbar\alpha_{i+1} = \sqrt{2m^*\left[eV_b - e\left(d + \frac{3w}{2}\right)F_i - \epsilon\right]},$$

(A.2)

(we have not distinguished between the electron effective masses at barriers and wells), and μ_i is the chemical potential of the ith well measured from the bottom thereof. The chemical potential is related to the electron density n_i by means of

$$n_i(\mu_i) = \frac{m^* k_B T}{\pi\hbar^2}\int_0^\infty A_{C1}(\epsilon)\ln\left[1 + \exp\left(\frac{\mu_i - \epsilon}{k_B T}\right)\right]d\epsilon. \tag{A.3}$$

We would like to obtain the tunnelling current density as a function of n_i, n_{i+1}, and F_i. It is difficult to obtain an analytical approximate expression because there are many small parameters entering the previous formulae. In [12], we argued that at low or high temperatures, $J_{i\to i+1} \approx n_i f(F_i) - n_{i+1}g(F_i)$, and the functions f and g could be calculated by fitting to numerical data. Here we shall study two special limits, $\gamma \ll k_B T \ll \Delta\epsilon$ and $k_B T \ll \gamma \ll \Delta\epsilon$, where $\Delta\epsilon = eF_i l - \mathcal{E}_{Cj} + \mathcal{E}_{C1}$ is representative of the energy differences appearing in the previous expressions. Clearly, these two limits are sensible for weakly coupled SL but they break down at low fields for tunnelling between the first subbands of adjacent wells. In common experimental situations, $\gamma \approx 10$ meV (that is 116 K), $\Delta\epsilon \approx 100$ meV, and $T = 4$ K, so the second limit is realized [40].

If $\gamma \ll \Delta\epsilon$ and $T > 0$, $A_{C1}(\epsilon) \sim \delta(\epsilon - \mathcal{E}_{C1})$ in (A.3), which then becomes

$$n_i(\mu_i) \sim \frac{m^* k_B T}{\pi\hbar^2}\ln\left[1 + \exp\left(\frac{\mu_i - \mathcal{E}_{C1}}{k_B T}\right)\right]. \tag{A.4}$$

This trick cannot be repeated in (A.1) for we would obtain a result proportional to $\delta(0)$. However, we can separate the integrals as

$$\int_0^\infty = \int_{\mathcal{E}_{C1}-\delta}^{\mathcal{E}_{C1}+\delta} + \int_0^{\mathcal{E}_{C1}-\delta} + \int_{\mathcal{E}_{C1}+\delta}^\infty. \tag{A.5}$$

Clearly, these integrals are negligible unless $\Delta\epsilon$ is very small compared to a representative energy scale: the subbands have to be almost in resonance for tunnelling to be significant. We will choose δ such that $\gamma \ll \delta \ll \Delta\epsilon$. Then we approximate all the functions in the integral from $\mathcal{E}_{C1} - \delta$ to $\mathcal{E}_{C1} + \delta$ by their value at $\epsilon = \epsilon_{C1}$ except for the two Lorentzians. The relative error involved is of order $\gamma\delta/(\Delta\epsilon)^2 \ll 1$. Notice that this error is small unless we want to explore $C1$–$C1$ tunnelling at zero field, in which case $\Delta\epsilon = 0$. Now we approximate the integral of the two Lorentzians from $\mathcal{E}_{C1} - \delta$ to $\mathcal{E}_{C1} + \delta$ by their integral from $-\infty$ to ∞ and use the exact formula

$$\int_{-\infty}^\infty A_{C1}(\epsilon)A_{Cj}(\epsilon + eF_i l)\,d\epsilon = \frac{(\gamma_{C1} + \gamma_{Cj})/\pi}{(\mathcal{E}_{C1} - \mathcal{E}_{Cj} + eF_i l)^2 + (\gamma_{C1} + \gamma_{Cj})^2}. \tag{A.6}$$

The relative errors involved in this approximation are of order γ/δ, and so are the additional relative errors if we also ignore all the integrals in (A.5) compared to the first one. The resulting tunnelling current is

$$J_{i \to i+1} = \frac{\hbar k_B T}{2m^*} \sum_{j=1}^{n} \frac{\frac{\gamma_{C1}+\gamma_{Cj}}{\pi} \mathcal{T}_i(\mathcal{E}_{C1})}{(\mathcal{E}_{C1} - \mathcal{E}_{Cj} + eF_i l)^2 + (\gamma_{C1} + \gamma_{Cj})^2} \ln\left[\frac{1 + \exp(\frac{\mu_i - \mathcal{E}_{C1}}{k_B T})}{1 + \exp(\frac{\mu_{i+1} - eF_i l - \mathcal{E}_{C1}}{k_B T})}\right]. \quad \text{(A.7)}$$

We can now eliminate the chemical potentials in favour of the electron densities by means of (A.4), with the result

$$J_{i \to i+1} = \sum_{j=1}^{n} \frac{\frac{\hbar^3(\gamma_{C1}+\gamma_{Cj})}{2m^{*2}} \mathcal{T}_i(\mathcal{E}_{C1})}{(\mathcal{E}_{C1} - \mathcal{E}_{Cj} + eF_i l)^2 + (\gamma_{C1} + \gamma_{Cj})^2}$$
$$\times \left\{ n_i - \frac{m^* k_B T}{\pi \hbar^2} \ln\left[1 + \exp\left(-\frac{eF_i l}{k_B T}\right)\left(\exp\left(\frac{\pi \hbar^2 n_{i+1}}{m^* k_B T}\right) - 1\right)\right]\right\}. \quad \text{(A.8)}$$

This expression is of the same form as that used in [3, 83]. It is not well justified for low fields and $C1$–$C1$ tunnelling, but it yields a useful analytical formula that can be used with greater ease than the complete integral in (A.1). Equivalently, equation (A.8) can be written as

$$J_{i \to i+1} = \frac{v^{(f)}(F_i)}{l}\left\{ n_i - \frac{m^* k_B T}{\pi \hbar^2} \ln\left[1 + \exp\left(-\frac{eF_i l}{k_B T}\right)\left(\exp\left(\frac{\pi \hbar^2 n_{i+1}}{m^* k_B T}\right) - 1\right)\right]\right\}, \quad \text{(A.9)}$$

$$v^{(f)} = \sum_{j=1}^{n} \frac{\frac{\hbar^3 l(\gamma_{C1}+\gamma_{Cj})\mathcal{T}_i(\mathcal{E}_{C1})}{2m^{*2}}}{(\mathcal{E}_{C1} - \mathcal{E}_{Cj} + eF_i l)^2 + (\gamma_{C1} + \gamma_{Cj})^2}. \quad \text{(A.10)}$$

In the limit $k_B T \gg \pi \hbar^2 n_{i+1}/m^* \approx \pi \hbar^2 N_D^w/m^*$, we can approximate (A.8) by

$$J_{i \to i+1} = \frac{v^{(f)}(F_i)}{l}(n_i - n_{i+1} e^{-\frac{eF_i l}{k_B T}}). \quad \text{(A.11)}$$

Notice that equation (A.11) yields the DDD model with analytic formulae for the drift velocity and diffusion coefficient:

$$v(F_i) = v^{(f)}(F_i)\left(1 - \exp\left(-\frac{eF_i l}{k_B T}\right)\right), \quad \text{(A.12)}$$

$$D(F_i) = v^{(f)}(F_i)l \exp\left(-\frac{eF_i l}{k_B T}\right), \quad \text{(A.13)}$$

where $v^{(f)}(F_i)$ is given by equation (A.10); see the insets in figure 5. Notice that the drift velocity (A.12) is somewhat similar to the Lorentzian dependence given by the simpler theory of Kazarinov and Suris [41]. Our additional prefactor in equation (A.10) yields a more complicated field dependence in our formulae. Our drift velocity is also similar to the escape time formula used by Rogozia and Grahn to give an estimation of the frequency of current self-oscillations [66], provided more precise expressions for $\mathcal{T}_i$ (with different electron masses at wells and barriers) are used.

In the opposite limit $k_B T \ll \pi \hbar^2 n_{i+1}/m^* \approx \pi \hbar^2 N_D^w/m^*$, equation (A.8) becomes

$$J_{i \to i+1} = \frac{v^{(f)}(F_i)}{l}\left[n_i - \left(n_{i+1} - \frac{m^* eF_i l}{\pi \hbar^2}\right)\theta\left(n_{i+1} - \frac{m^* eF_i l}{\pi \hbar^2}\right)\right]. \quad \text{(A.14)}$$

Here $\theta(x)$ is the Heaviside unit step function and we have ignored an exponentially small term for $n_{i+1} < m^* eF_i l/(\pi \hbar^2)$. The same formula can be obtained directly from equations (A.1) and (A.3) in the limit $k_B T \ll \gamma \ll \Delta\epsilon$, after some algebra.

Similar approximations can be used to obtain analytical formulae for the boundary conditions. The tunnelling current from the emitter contact becomes

$$J_{0\to 1} \approx j_e^{(f)}(F_0) - \frac{n_1}{l}w^{(b)}(F_0), \tag{A.15}$$

$$j_e^{(f)}(F) = \sum_{j=1}^{n} \frac{16\alpha_0^2 k_0 k_1^2 (k_0^2 + \alpha_0^2)^{-1}(k_1^2 + \alpha_0^2)^{-1}}{(w + \alpha_0^{-1} + \alpha_1^{-1})e^{2\alpha_0 d}} \theta\left(\mathcal{E}_{Cj} - eF\left(l + \frac{w}{2}\right)\right)$$

$$\times \frac{k_B T}{2\pi\hbar} \ln\left(1 + \exp\left(\frac{\epsilon_F + eF(l + w/2) - \mathcal{E}_{Cj}}{k_B T}\right)\right), \tag{A.16}$$

$$w^{(b)}(F) = \frac{8\hbar k_0 k_1^2 \alpha_0^2 l (k_0^2 + \alpha_0^2)^{-1}e^{-2\alpha_0 d}}{m^*(w + \alpha_0^{-1} + \alpha_1^{-1})(k_1^2 + \alpha_0^2)} \theta\left(\mathcal{E}_{C1} - eF\left(l + \frac{w}{2}\right)\right), \tag{A.17}$$

where k_1, α_0, etc are given by (A.2) with $i = 1$ and $\epsilon = \mathcal{E}_{Cj}$. The tunnelling current to the collector is

$$J_{N\to N+1} \approx \frac{n_N}{l}w^{(f)}(F_N), \tag{A.18}$$

$$w^{(f)}(F) = \frac{8\hbar\alpha_N^2 k_N^2 k_{N+1} l (k_N^2 + \alpha_N^2)^{-1}e^{-2\alpha_N d}}{m^*(k_{N+1}^2 + \alpha_N^2)(w + \alpha_N^{-1} + \alpha_{N-1}^{-1})}, \tag{A.19}$$

where k_N, α_N, etc are given by (A.2) with $i = N$ and $\epsilon = \mathcal{E}_{C1}$.

Appendix B. Sequential tunnelling current and continuum limit

Often it is convenient to work with the full sequential tunnelling current given by equation (A.8) instead of working with the DDD approximation. The theory described in this paper is based upon studying wavefronts under current bias and it can be easily extended to the general case. It is clear how to do this for the active well theory, and we shall study now the motion of wavefronts in the continuum limit. First of all, let us nondimensionalize the discrete model with the tunnelling current given by equation (A.8), as explained in section 5. The result is

$$\frac{dE_i}{dt} + v^{(f)}(E_i)\{n_i - \tau \ln[1 + e^{-\alpha E_i/\tau}(e^{n_{i+1}/\tau} - 1)]\} = J, \tag{B.1}$$

where $v^{(f)}(E_i) = v^{(f)}(F_M E_i)/v_M$ is the dimensionless forward velocity, and $\tau = m^* k_B T/(\pi\hbar^2 N_D^w)$ and $\alpha = eF_M l m^*/(\pi\hbar^2 N_D^w)$ are two new dimensionless parameters. For the first plateau of the 9/4 SL at $T = 5$ K, $\tau = 0.076$ and $\alpha = 1.6$. In the continuum limit, equations (3.12) and (B.1) yield the following strongly nonlinear hyperbolic equation:

$$\frac{\partial E}{\partial t} + v^{(f)}(E)\left\{1 + \frac{\partial E}{\partial x} - \tau \ln[1 + e^{-\alpha E/\tau}(e^{(1+\partial E/\partial x)/\tau} - 1)]\right\} = J, \tag{B.2}$$

up to $O(\nu)$ terms. This equation needs to be supplemented by a law for the velocity of shock waves, $V(E_+, E_-)$. To find it, we first observe that, inside the shock wave, $(n_{i+1}/\tau) \gg 1$, so we may approximate the logarithmic term in equation (B.1) by its zero-temperature approximation $(n_{i+1} - \alpha E_i)\theta(n_{i+1} - \alpha E_i) + \tau e^{-|n_{i+1} - \alpha E_i|/\tau}$. Keeping the leading order only, we obtain

$$V\sum \frac{E_i - E_{i-1}}{v^{(f)}(E_i)} \sim -\sum \frac{\nu\, dE_i/dt}{v^{(f)}(E_i)} \sim \sum \nu\left[n_i - \frac{(n_{i+1} - \alpha E_i)\theta(n_{i+1} - \alpha E_i) + J}{v^{(f)}(E_i)}\right]$$

$$\sim \sum(E_i - E_{i-1}) - \sum \frac{(E_{i+1} - E_i)\theta(1 - \alpha E_i)}{v^{(f)}(E_i)}$$

$$+ \nu\sum \frac{v^{(f)}(E_i) - J + (\alpha E_i - 1)\theta(1 - \alpha E_i)}{v^{(f)}(E_i)}.$$

Equivalently,

$$V\sum \frac{E_i - E_{i-1}}{v^{(f)}(E_i)} \sim \sum \frac{v^{(f)}(E_i) - \theta(1 - \alpha E_i)}{v^{(f)}(E_i)}(E_{i+1} - E_i)$$

$$+ \nu\sum \frac{v^{(f)}(E_i) - J + (\alpha E_i - 1)\theta(1 - \alpha E_i)}{v^{(f)}(E_i)}.$$

The numerator of the last term becomes zero outside the wavefront, which means that this term is of order ν and it can be ignored in the continuum limit $\nu \to 0$. Approximating the Riemann sums by integrals, we therefore obtain

$$V(E_+, E_-) = \frac{\int_{E_-}^{E_+} \frac{v^{(f)}(E) - \theta(1 - \alpha E)}{v^{(f)}(E)} \, \mathrm{d}E}{\int_{E_-}^{E_+} \frac{\mathrm{d}E}{v^{(f)}(E)}}. \tag{B.3}$$

References

[1] Aguado R, Platero G, Moscoso M and Bonilla L L 1997 *Phys. Rev.* B **55** R16 053
[2] Allan G, Bastard G, Boccara N, Lannoo M and Voos M (ed) 1986 *Heterojunctions and Semiconductor Superlattices* (Berlin: Springer)
[3] Amann A, Wacker A, Bonilla L L and Schöll E 2001 *Phys. Rev.* E **63** 066207
[4] Amann A, Schlesner J, Wacker A and Schöll E 2001 *Preprint* cond-mat/0112215
[5] Bastard G 1988 *Wave Mechanics Applied to Semiconductor Superlattices* (New York: Halsted)
[6] Bender C M and Orszag S A 1978 *Advanced Mathematical Methods for Scientists and Engineers* (New York: McGraw-Hill)
[7] Bonilla L L 1987 *J. Stat. Phys.* **46** 659
[8] Bonilla L L, Galán J, Cuesta J A, Martínez F C and Molera J M 1994 *Phys. Rev.* B **50** 8644
[9] Bonilla L L 1995 *Nonlinear Dynamics and Pattern Formation in Semiconductors and Devices* ed F-J Niedernostheide (Berlin: Springer) p 1
[10] Bonilla L L, Kindelan M, Moscoso M and Venakides S 1997 *SIAM J. Appl. Math.* **57** 1588
[11] Bonilla L L, Cantalapiedra I R, Gomila G and Rubí J M 1997 *Phys. Rev.* E **56** 1500
[12] Bonilla L L, Platero G and Sánchez D 2000 *Phys. Rev.* B **62** 2786
[13] Bonilla L L, Sánchez O and Soler J 2002 *Phys. Rev.* B **65** at press (cond-mat/0201500)
[14] Braun O M and Kivshar Yu S 1998 *Phys. Rep.* **306** 1
[15] Bulashenko O M and Bonilla L L 1995 *Phys. Rev.* B **52** 7849
[16] Bulashenko O M, García M J and Bonilla L L 1996 *Phys. Rev.* B **53** 10 008
[17] Bulashenko O M, Luo K J, Grahn H T, Ploog K H and Bonilla L L 1999 *Phys. Rev.* B **60** 5694
[18] Butcher P N 1967 *Rep. Prog. Phys.* **30** 97
[19] Cantalapiedra I R, Bergmann M J, Bonilla L L and Teitsworth S W 2001 *Phys. Rev.* E **63** 056216
[20] Cao J C and Lei X L 1999 *Phys. Rev.* B **60** 1871
[21] Cao J C, Liu H C and Lei X L 2000 *Phys. Rev.* B **61** 5546
[22] Cao J C, Liu H C and Lei X L 2000 *J. Appl. Phys.* **87** 2867
[23] Cao J C, Liu H C, Lei X L and Perera A G U 2001 *Phys. Rev.* B **63** 115308
[24] Carpio A, Bonilla L L, Wacker A and Schöll E 2000 *Phys. Rev.* E **61** 4866
[25] Carpio A, Chapman S J, Hastings S and McLeod J B 2000 *Eur. J. Appl. Math.* **11** 399
[26] Carpio A and Bonilla L L 2001 *Phys. Rev. Lett.* **86** 6034
[27] Carpio A, Bonilla L L and Dell Acqua G 2001 *Phys. Rev.* E **64** 036204
[28] Carpio A, Bonilla L L and Luzón A *Phys. Rev.* E 2002 **66** 035207
[29] Choi K K, Levine B F, Malik R J, Walker J and Bethea C G 1987 *Phys. Rev.* B **35** 4172
[30] Gerde E and Marder M 2001 *Nature* **413** 285
[31] Grahn H T, Schneider H and von Klitzing K 1990 *Phys. Rev.* B **41** 2890
[32] Grahn H T, Haug R J, Müller W and Ploog K 1991 *Phys. Rev. Lett.* **67** 1618
[33] Grahn H T (ed) 1995 *Semiconductor Superlattices: Growth and Electronic Properties* (Singapore: World Scientific)
[34] Grahn H T, Kastrup J, Ploog K, Bonilla L L, Galán J, Kindelan M and Moscoso M 1995 *Japan. J. Appl. Phys.* **34** 4526
[35] Grüner G 1988 *Rev. Mod. Phys.* **60** 1129
[36] Higuera F J and Bonilla L L 1992 *Physica* D **57** 161
[37] Ivchenko E L and Pikus G 1995 *Superlattices and Other Heterostructures* (Berlin: Springer)
[38] Kantelhardt J W, Grahn H T, Ploog K H, Moscoso M, Perales A and Bonilla L L 1997 *Phys. Status Solidi* b **204** 500
[39] Kastrup J, Grahn H T, Ploog K, Prengel F, Wacker A and Schöll E 1994 *Appl. Phys. Lett.* **65** 1808
[40] Kastrup J, Grahn H T, Hey R, Ploog K, Bonilla L L, Kindelan M, Moscoso M, Wacker A and Galán J 1997 *Phys. Rev.* B **55** 2476
[41] Kazarinov R F and Suris R A 1972 *Fiz. Tekh. Poluprov.* **6** 148 (Engl. transl. 1972 *Sov. Phys.–Semicond.* **6** 120)

[42] Keener J P 1987 *SIAM J. Appl. Math.* **47** 556
[43] Knight B W and Peterson G A 1966 *Phys. Rev.* **147** 617
[44] Laikhtman B 1991 *Phys. Rev.* B **44** 11 260
[45] Laikhtman B and Miller D 1993 *Phys. Rev.* B **48** 5395
[46] Li C-Y, Sun B-Q, Jiang D-S and Wang J-N 2001 *Semicond. Sci. Technol.* **16** 239
[47] Likharev K K, Bakhvalov N S, Kazacha G S and Serdyukova S I 1989 *IEEE Trans. Magn.* **25** 1436
[48] Luo K J, Grahn H T, Ploog K H and Bonilla L L 1998 *Phys. Rev. Lett.* **81** 1290
[49] Luo K J, Grahn H T and Ploog K H 1998 *Phys. Rev.* B **57** R6838
[50] Luo K J, Friedland K-J, Grahn H T and Ploog K H 2000 *Phys. Rev.* B **61** 4477
[51] Luo K J, Friedland K-J, Grahn H T and Ploog K H 2000 *Appl. Phys. Lett.* **76** 2913
[52] Merlin R, Kwok S H, Norris T B, Grahn H T, Ploog K, Bonilla L L, Galán J, Cuesta J A, Martínez F C and
       Molera J M 1995 *Proc. 22nd ICPS* ed D J Lockwood (Singapore: World Scientific) p 1039
[53] Miller D A B, Chemla D S, Damen T C, Gossard A C, Wiegmann W, Wood T H and Burrus C A 1984 *Phys.
       Rev. Lett.* **53** 2173
[54] Mosekilde E, Feldberg R, Knudsen C and Himdsholm M 1990 *Phys. Rev.* B **41** 2298
[55] Moscoso M, Galán J and Bonilla L L 2000 *SIAM J. Appl. Math.* **60** 2029
[56] Murray J D 1970 *J. Fluid Mech.* **44** 315
[57] Nabarro F R N 1987 *Theory of Crystal Dislocations* (New York: Dover)
[58] Ohtani N, Egami N, Grahn H T, Ploog K H and Bonilla L L 1998 *Phys. Rev.* B **58** R7528
[59] Ohtani N, Egami N, Grahn H T and Ploog K H 2000 *Phys. Rev.* B **61** R5097
[60] Oshio K and Yahata H 1993 *J. Phys. Soc. Japan* **62** 3639
[61] Patra M, Schwarz G and Schöll E 1998 *Phys. Rev.* B **57** 1824
[62] Perales A, Bonilla L L, Moscoso M and Galán J 2001 *Int. J. Bifurcation Chaos* **11** 2817
[63] Prengel F, Wacker A and Schöll E 1994 *Phys. Rev.* B **50** 1705
[64] Rogozia M, Teitsworth S W, Grahn H T and Ploog K H 2001 *Phys. Rev.* B **64** 041308(R)
[65] Rogozia M, Teitsworth S W, Grahn H T and Ploog K H 2001 *Phys. Rev.* B **65** at press
[66] Rogozia M and Grahn H T 2001 *Appl. Phys.* A **73** 459
[67] Sánchez D, Moscoso M, Bonilla L L, Platero G and Aguado R 1999 *Phys. Rev.* B **60** 4489
[68] Sánchez D, Platero G and Bonilla L L 2001 *Phys. Rev.* B **63** 201306(R)
[69] Sánchez D, Platero G and Bonilla L L 2001 *Phys. Rev.* B **64** 115311
[70] Schneider H, von Klitzing K and Ploog K H 1989 *Superlatt. Microstruct.* **5** 383
[71] Schöll E, Schwarz G, Patra M, Prengel F and Wacker A 1996 *Hot Carriers in Semiconductors* ed K Hess,
       J P Leburton and U Ravaioli (New York: Plenum) p 177
[72] Schöll E, Schwarz G and Wacker A 1998 *Physica* B **249–51** 961
[73] Sibille A, Palmier J F, Mollot F, Wang H and Esnault J C 1989 *Phys. Rev.* B **39** 6272
[74] Sibille A 1996 *Semiconductor Superlattices: Growth and Electronic Properties* ed H T Grahn (Singapore:
       World Scientific) p 29
[75] Slepyan L I 1981 *Dokl. Akad. Nauk SSSR* **258** 561 (Engl. transl. 1981 *Sov. Phys.–Dokl.* **26** 538)
[76] Smith D L and Mailhiot C 1990 *Rev. Mod. Phys.* **62** 173
[77] Steuer H, Wacker A, Schöll E, Ellmauer M, Schomburg E and Renk K F 2000 *Appl. Phys. Lett.* **76** 2059
[78] Sun B, Wang J, Ge W, Wang Y, Jiang D, Zu H, Wang H, Deng Y and Feng S 1999 *Phys. Rev.* B **60** 8866
[79] Sun B, Wang J N, Jiang D S, Wu J Q, Wang Y Q and Ge W K 2000 *Physica* B **279** 220
[80] Wacker A, Schwarz G, Prengel F, Schöll E, Kastrup J and Grahn H T 1995 *Phys. Rev.* B **52** 13 788
[81] Wacker A, Moscoso M, Kindelan M and Bonilla L L 1997 *Phys. Rev.* B **55** 2466
[82] Wacker A 1998 *Theory and Transport Properties of Semiconductor Nanostructures* ed E Schöll (New York:
       Chapman and Hall) ch 10
[83] Wacker A 2002 *Phys. Rep.* **357** 1
[84] Wang J N, Sun B Q, Wang X R, Wang Y, Ge W and Wang H 1999 *Appl. Phys. Lett.* **75** 2620
[85] Wang X R, Wang J N, Sun B Q and Jiang D S 2000 *Phys. Rev.* B **61** 7261
[86] van der Zant H S J, Orlando T P, Watanabe S and Strogatz S H 1995 *Phys. Rev. Lett.* **74** 174
[87] Zhang Y, Kastrup J, Klann R, Ploog K and Grahn H T 1996 *Phys. Rev. Lett.* **77** 3001
[88] Zhang Y, Klann R, Grahn H T and Ploog K 1997 *Superlatt. Microstruct.* **21** 565